Cell Reports

Article

Sublayer- and cell-type-specific neurodegenerative transcriptional trajectories in hippocampal sclerosis

Graphical abstract

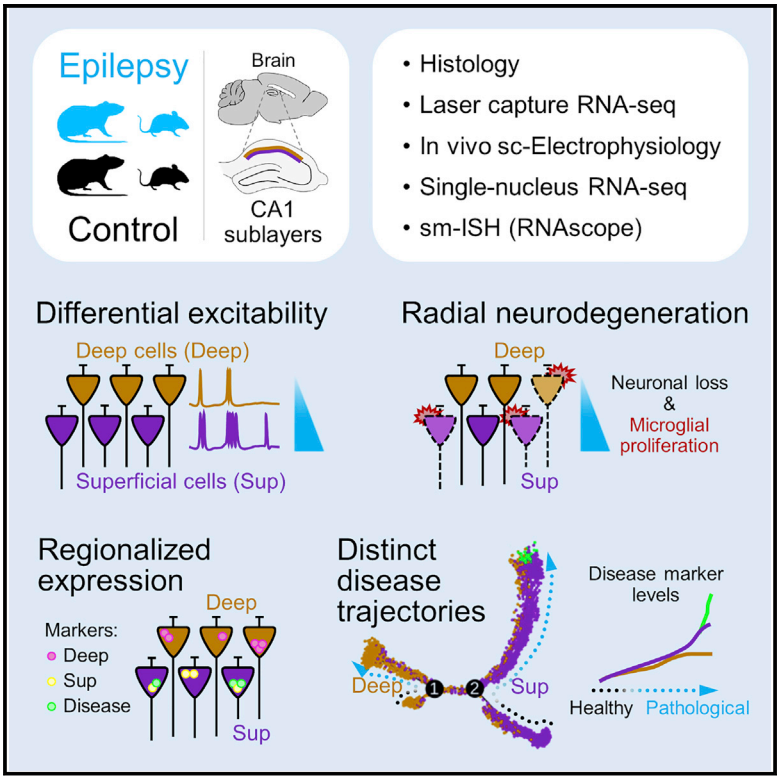

Authors

Elena Cid, Angel Marquez-Galera, Manuel Valero, ..., Angel Barco, Jose P. Lopez-Atalaya, Liset M. de la Prida

Correspondence

jose.lopezatalaya@csic.es (J.P.L.-A.), lmprida@cajal.csic.es (L.M.d.l.P.)

In brief

Cid et al. use a combination of techniques from single-cell recordings *in vivo* to bulk tissue and single-nucleus RNA-seq to reveal cell-type-specific segregation of neurodegenerative and epileptogenic processes in experimental epilepsy. They find that segregated disease-specific gene expression changes run differentially across cell types and sublayers of the hippocampal CA1 region.

Highlights

- Superficial CA1 pyramidal neurons are overactive in epileptic rodents
- Neurodegeneration-related gene signatures progress radially in the epileptic CA1
- Larger vulnerability of superficial CA1 pyramidal cells in experimental epilepsy
- Cell-type-specific disease trajectories characterize hippocampal sclerosis

Cid et al., 2021, Cell Reports *35*, 109229
June 8, 2021
https://doi.org/10.1016/j.celrep.2021.109229

CellPress

Cell Reports

CellPress
OPEN ACCESS

Article

Sublayer- and cell-type-specific neurodegenerative transcriptional trajectories in hippocampal sclerosis

Elena Cid,[1,8] Angel Marquez-Galera,[2,8] Manuel Valero,[1] Beatriz Gal,[1,3] Daniel C. Medeiros,[1] Carmen M. Navarron,[2] Luis Ballesteros-Esteban,[1] Rita Reig-Viader,[4,5] Aixa V. Morales,[1] Ivan Fernandez-Lamo,[1] Daniel Gomez-Dominguez,[1] Masaaki Sato,[6] Yasunori Hayashi,[6,7] Àlex Bayés,[4,5] Angel Barco,[2] Jose P. Lopez-Atalaya,[2,*] and Liset M. de la Prida[1,9,*]

[1]Instituto Cajal, CSIC, 28002 Madrid, Spain
[2]Instituto de Neurociencias, Universidad Miguel Hernández-Consejo Superior de Investigaciones Científicas (UMH-CSIC), 03550 Sant Joan d'Alacant, Alicante, Spain
[3]Universidad Europea de Madrid, 28670 Villaviciosa de Odón, Madrid, Spain
[4]Institut d'Investigació Biomèdica San Pau, 08041 Barcelona, Spain
[5]Universitat Autònoma de Barcelona, 08193 Bellaterra, Cerdanyola del Vallès, Spain
[6]RIKEN Brain Science Institute, Wako, 351-0198 Saitama, Japan
[7]Department of Pharmacology, Kyoto University Graduate School of Medicine, 606-8501 Kyoto, Japan
[8]These authors contributed equally
[9]Lead contact
*Correspondence: jose.lopezatalaya@csic.es (J.P.L.-A.), lmprida@cajal.csic.es (L.M.d.l.P.)
https://doi.org/10.1016/j.celrep.2021.109229

SUMMARY

Hippocampal sclerosis, the major neuropathological hallmark of temporal lobe epilepsy, is characterized by different patterns of neuronal loss. The mechanisms of cell-type-specific vulnerability and their progression and histopathological classification remain controversial. Using single-cell electrophysiology *in vivo* and immediate-early gene expression, we reveal that superficial CA1 pyramidal neurons are overactive in epileptic rodents. Bulk tissue and single-nucleus expression profiling disclose sublayer-specific transcriptomic signatures and robust microglial pro-inflammatory responses. Transcripts regulating neuronal processes such as voltage channels, synaptic signaling, and cell adhesion are deregulated differently by epilepsy across sublayers, whereas neurodegenerative signatures primarily involve superficial cells. Pseudotime analysis of gene expression in single nuclei and *in situ* validation reveal separated trajectories from health to epilepsy across cell types and identify a subset of superficial cells undergoing a later stage in neurodegeneration. Our findings indicate that sublayer- and cell-type-specific changes associated with selective CA1 neuronal damage contribute to progression of hippocampal sclerosis.

INTRODUCTION

Epilepsies are brain disorders characterized by an enduring predisposition to generate seizures with emotional and cognitive associated comorbidities. Despite significant therapeutic advances, one-third of affected individuals remain resistant to pharmacotherapy (Chen et al., 2018). Temporal lobe epilepsy (TLE), the most prevalent form of pharmacoresistant epilepsy, is frequently associated with hippocampal sclerosis (Blümcke et al., 2013). Hippocampal sclerosis is characterized by specific patterns of neuronal loss affecting different hippocampal subfields from the CA1 to CA3/4 areas, the hilus of the dentate gyrus, and superficial layers of the entorhinal cortex (Blümcke et al., 2009; Du et al., 1995; de Lanerolle et al., 2003). Factors such as epilepsy history, age of onset, and the relationship with early precipitating events may all influence the degree and severity of hippocampal sclerosis (Davies et al., 1996).

The most common form of hippocampal sclerosis (type 1; 60%–80% of TLE cases) shows severe neuronal loss of CA1, CA3, and CA4 pyramidal neurons and milder loss in CA2, with variability along the anteroposterior axis (Blümcke et al., 2013; Wyler et al., 1992). Other cell types, including microglia and astrocytes, are also affected (Blümcke et al., 2013; Morin-Brureau et al., 2018). In contrast, type 2 hippocampal sclerosis (10%–20% of cases) is associated with predominant CA1 neurodegeneration and minimal loss in other regions (Blümcke et al., 2013). Given the disparities between clinical series, there is no consensus on whether neuronal loss progresses over time (Blümcke et al., 2009; Davies et al., 1996). In addition, individual variabilities and anatomical inhomogeneities complicate classification (Coras et al., 2014; Rodrigues et al., 2015; Saghafi et al., 2018). For instance, patchy neuronal loss has been described in the CA1 region in some cases, whereas in others, it seems to adopt a more laminar profile

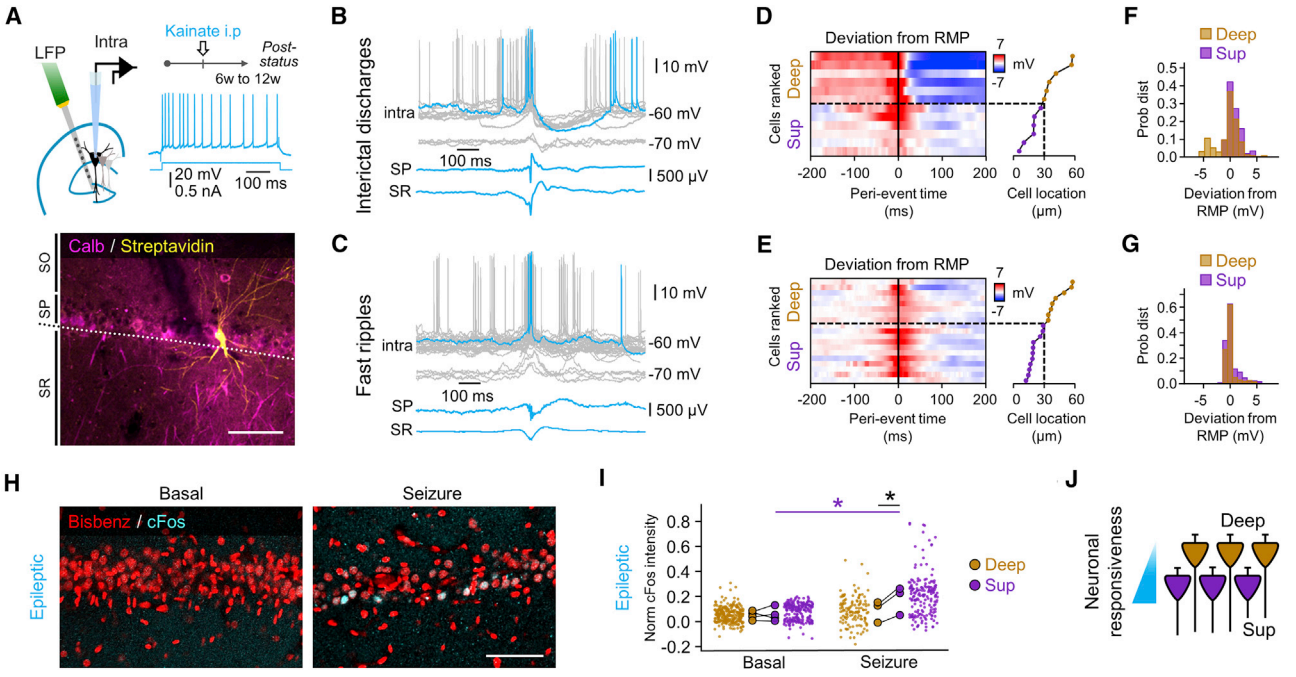

Figure 1. Differential responses of CA1 pyramidal cells during epileptiform activities

(A) Intracellular and multi-site local field potential (LFP) recordings from epileptic rats. Cells were identified with streptavidin and tested against Calbindin. Scale bar, 100 µm. SO, *stratum oriens*; SP, *stratum pyramidale*; SR; *stratum radiatum*.

(B) Intracellular activity during IID at different membrane potentials (gray traces). Traces are aligned by the peak of IID recorded at the SR. HFOs were recorded at the SP.

(C) Responses of the cell shown in (A) during SPW fast ripples.

(D) Deviation from the resting membrane potential (RMP) recorded in individual cells during IIDs (n = 12 cells). Red colors reflect depolarization and blue hyperpolarization. Cells are ranked by their distance to the SR and classified as deep and superficial (Sup) (subplot at right). The discontinuous line marks sublayer limits.

(E) Same as in D for SPW-fast ripples (n = 19 cells).

(F) Mean membrane potential responses around IID events showed differences between deep and Sup cells (Friedman χ^2 [1,333] = 28.7, $p < 0.001$). Data are from 6 deep and 6 Sup CA1 pyramidal cells.

(G) Same as in (G) for SPW fast ripple events. Note the larger after-event depolarization in Sup cells (Friedman χ^2 [1,333] = 14.67, $p < 0.0001$). Data are from 8 deep and 11 Sup CA1 pyramidal cells.

(H) cFos immunoreactivity in representative CA1 sections from one rat exhibiting bilateral forelimb clonus after sound stimulation (seizure) versus a non-stimulated epileptic rat with no observed seizure (basal). Scale bar, 80 µm.

(I) Intensity of c-Fos from all pyramidal cells in one confocal section per rat (small dots) and mean data per animal (larger dots). Significant interaction was confirmed for animals between groups and sublayers ($p = 0.0044$; n = 4 epileptic basal, n = 3 epileptic seizures). Post hoc differences: *$p < 0.05$.

(J) Schematic of electrophysiological and histopathological findings.

(Prada Jardim et al., 2018). In some affected individuals, cell loss concentrates in the CA4 region and the dentate gyrus and is frequently integrated in dual pathologies; e.g., TLE and malformations of cortical development, classified as type 3 hippocampal sclerosis (3%–7%) (Mathern et al., 1997). The mechanisms underlying specific vulnerability of diverse cells and their role in the histopathological landscape and clinical significance remain unknown.

Recent techniques and methods operating at single-cell resolution point to an exquisite cell-type-specific organization that is instrumental for brain function (Habib et al., 2016; Zeisel et al., 2015). In the hippocampus, the CA1 region is organized radially in two distinct sublayers with characteristic gene expression gradients along the anteroposterior and proximodistal axes (Cembrowski et al., 2016a; Dong et al., 2009; Slomianka et al., 2011). Functionally, superficial (closer to *radiatum*) and deep (closer to *oriens*) CA1 pyramidal neurons project differentially and diverge in their participation of sharp-wave ripple activity, theta-gamma oscillations, and behavioral-cognitive correlates (Soltesz and Losonczy, 2018; Valero and de la Prida, 2018). In spite of data suggesting critical regionalization of CA1 neuronal responses to ischemia, anoxia, and epilepsy (Morris et al., 1995; Valero et al., 2017; Wittner et al., 2002), little is known about their clinical relevance and potential relationship with neuronal vulnerability. Understanding the effect of cellular diversity and transcriptional changes in epilepsy progression may lend insights into more specific mechanisms toward new diagnostic and therapeutic opportunities (Pfisterer et al., 2020).

Here we combine gene expression profiling at the single-nucleus and microdissected tissue levels with single-cell electrophysiology to disclose epileptogenic and neurodegenerative

changes running differentially across CA1 sublayers in an experimental model of hippocampal sclerosis. Our study highlights the importance of leveraging cell type specificity to better understand the phenotypic complexities accompanying hippocampal sclerosis in epilepsy.

RESULTS

Large activity burden in superficial CA1 pyramidal cells during epileptiform activities

Single CA1 pyramidal cells were recorded intracellularly from anesthetized epileptic rats to evaluate their intrinsic excitability and activity during interictal discharges (IIDs), sharp-wave (SPW) fast ripples, and ictal discharges (Figures 1A–1C; Figures S1A and S1B). Recorded cells were identified post hoc (with streptavidin) and immunostained against Calbindin (Calb) to classify them as deep (negative) or superficial pyramidal cells (positive) (Figure 1A). SPW-associated high-frequency oscillation (HFO) events were detected automatically and classified as ripples (100–150 Hz), fast ripples (>150 Hz) and IID using amplitude and spectral information (Figures S1C and S1D), as before (Valero et al., 2017).

Intracellular activities recorded during IID events (n = 12 cells; Figure 1B) and SPW fast ripples (n = 19 cells; Figure 1C) were typically associated with consistent depolarization from the resting membrane potential (RMP), and firing of all pyramidal cells was examined (Figures 1D and 1E). A temporal analysis of membrane potential changes (30-ms bins) showed differences between cell types during both IID events (Figure 1F; Friedman χ^2 [1,333] = 28.7, $p < 0.001$) and SPW fast ripples (Figure 1G; Friedman χ^2 [1,333] = 14.67, $p < 0.0001$), with superficial cells consistently showing larger depolarization at the event peak. Post-event membrane potential responses recorded showed effect for the type of events ($F(2,57) = 7.17$, $p = 0.0018$), sublayer ($F(1,57) = 5.44$, $p = 0.0236$) and interaction ($F(2,57) = 4.89$, $p = 0.0113$). Post hoc Tukey tests confirmed significant smaller hyperpolarization ($p = 0.0020$) and a higher firing rate ($p = 0.045$) following IID events in superficial compared with deep cells. We found some minor differences of intrinsic excitability between cell types and groups (Table S1).

We reasoned that superficial pyramidal cells should be more steadily activated during seizures, given their poor post-event hyperpolarization. We exposed 3 epileptic rats to high-pitched sounds to promote convulsive seizures (pulses of 95–100 dB and 1- to 20-s duration at random intervals of 1–20 s during 10 min) (seizure group). This group was compared with 4 unstimulated epileptic rats without any observed clinical seizure (basal group). Animals were sacrificed after 1 h to evaluate expression of the immediate-early gene cFos (Figure 1H). Statistics per cell confirmed effects for interaction between groups and sublayer ($p < 0.0001$; 2-way ANOVA). Significant interaction was confirmed for animals ($p = 0.0044$) with post hoc differences between groups for superficial cells only ($p = 0.0395$) and between deep and superficial cells within the seizure group ($p = 0.0117$) (Figure 1I).

These results suggest higher responsiveness of superficial CA1 pyramidal cells during epileptiform activities in chronically epileptic rats (Figure 1J).

Sublayer regionalization of epilepsy-associated transcriptional responses

To investigate how the differential responsiveness of deep and superficial cells may relate with distinct transcriptional responses across sublayers, we performed RNA sequencing (RNA-seq) analysis of laser capture microdissection (LCM) samples from control (saline-injected) and epileptic rats (n = 3 replicates each; Figures 2A, S2A, and S2B; Table S2).

Analysis of LCM RNA-seq data revealed sublayer-specific genes common to control and epileptic animals (absolute $\log_2$ fold change [FC] > 0.5; adj. $p < 0.01$; Figure 2B; superficial versus deep samples). Among these, we retrieved *bona fide* marker genes of superficial (*Calb1*, *Grm1*, and *Syt17*) and deep CA1 pyramidal cells (*Ndst4*), consistent with previous data for mice (Cembrowski et al., 2016b, 2016a) (Figure S2C; see Figures S2D and S2E for validation by *in situ* hybridization). Sublayer gene expression analysis confirmed preserved regionalization in epileptic rats with only a subset of uncorrelated transcripts (FC > 0.5; adj. $p < 0.01$; Figure 2C, red dots; see Figure S2F for less stringent criteria: adj. $p < 0.1$). Strikingly, we found that some gene markers of other cell types in the hippocampus, including interneurons (*Sst*, *Vip*, and *Kit*), oligodendrocytes (*Mbp*, *Plp1*, and *Mobp*), astrocytes (*Aqp4*, *Gja1*, and *Gfap*), and homeostatic microglia (*Tgfbr1* and *Csf1r*), also exhibited sublayer differences, consistent with heterogeneous distribution of cell types across the CA1 radial axis (Figures 2B, 2C, and S2F) (see below).

Next, we investigated the transcriptional changes associated with epilepsy across CA1 sublayers (epileptic versus control samples per sublayer). We identified 103 significantly differentially expressed genes (DEGs) in the deep sublayer of epileptic versus control rats versus 376 DEGs in the superficial sublayer (FC > 0.5; adj. $p < 0.01$; Figure 2D). Although epilepsy-associated transcriptional changes run in similar directions in both sublayers (i.e., no counter-regulated genes), they were more exacerbated in the superficial CA1 (Figures 2D and S2H). Overall, we retrieved more upregulated than downregulated genes, particularly in the superficial (73% DEGs) versus the deep sublayer (57% DEGs) (Figure 2D, Venn diagrams on the right). Because of the small size of the gene set differentially regulated by epilepsy in the deep sublayer, a less stringent threshold was used to perform functional enrichment analysis with gene sets of equal sizes. We first required the genes to show a modest level of statistical significance (adj. $p < 0.1$) and ranked them by FC to retain the top 250 upregulated genes and top 250 downregulated genes. Functional enrichment analyses of these gene sets of equal size also revealed marked differences (Figure 2E).

Downregulated DEGs in epilepsy in the superficial CA1 sublayer show robust functional association with many Gene Ontology (GO) terms (adj. $p < 0.05$) linked to neuronal processes, such as synaptic transmission and neuron projection, including many well-known modulators of epileptogenic process, such as *Cacnb1*, *Cacnb4*, *Cacng2,* *Kcnq3*, *Kcnab1*, *Scn4b*, *Grin2a*, *Nptn*, and *Gria4* (Winden et al., 2015) (Figure 2E). Most of these Gene Ontology (GO) terms were significantly enriched only in the superficial CA1 sublayer (Figure 2E). Regarding upregulated genes in epilepsy, there were no GO terms significantly enriched using the gene set from the deep

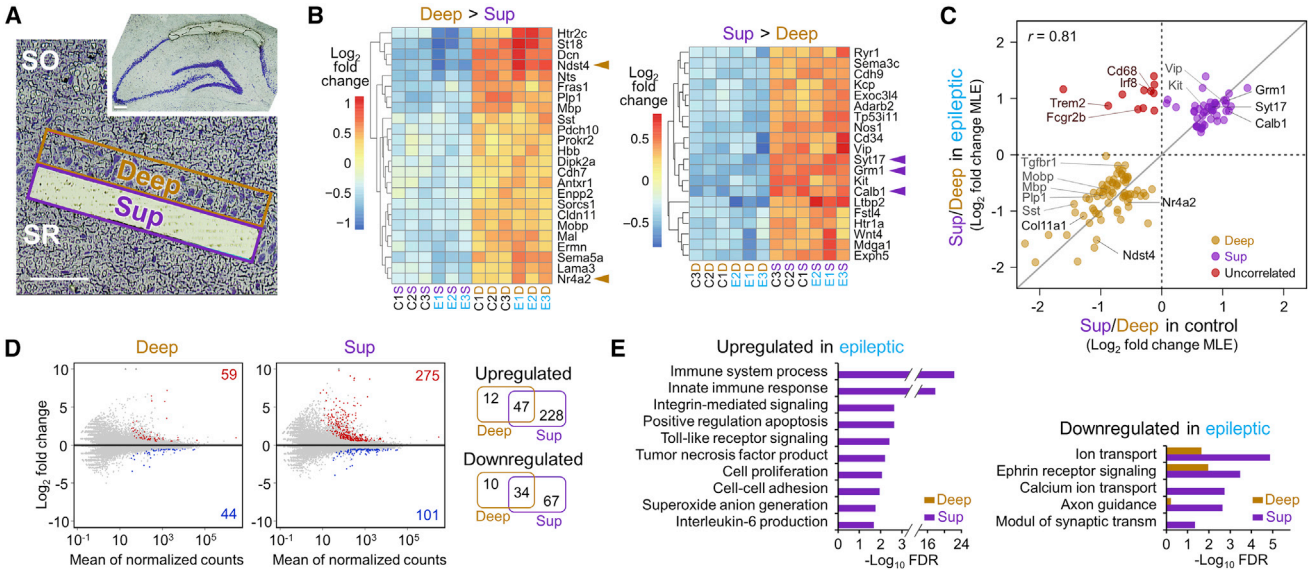

Figure 2. Bulk tissue gene expression profiling of the epileptic hippocampal area CA1 reveals regionalized transcriptional response

(A) Representative laser capture microdissection (LCM) sampling of the Sup CA1 sublayer. Scale bar, 100 μm.

(B) Heatmaps of DEGs in deep (left) and Sup CA1 sublayers (right) in three replicates from control (C) and epileptic (E) rats (FC > 0.5, adj. $p < 0.01$). Arrowheads point to *bona fide* gene markers of Sup (*Calb1*, *Grm1*, and *Syt17*) and deep (*Ndst4* and *Nr4a2*) pyramidal neurons. Note the presence of gene markers for interneurons (e.g., *Vip*, *Sst*, *Sema3c*, and *Kit*) and oligodendrocytes (*Plp1*, *Mbp*, *Mobp*, *Mal*, *Enpp2*, *Cldn11*, and *Ermn*).

(C) Scatterplot of DEGs between Sup and deep CA1 sublayers in control or epileptic rats (FC > 0.5, adj. $p < 0.01$). *Bona fide* gene markers of Sup (*Calb1*, *Grm1*, and *Syt17*) and deep (*Ndst4*, *Nr4a2*, *and Col11a1*) pyramidal neurons are highlighted (black text and bold font). Also shown are marker genes for interneurons (*Sst*, *Vip*, and *Kit*), oligodendrocytes (*Mbp*, *Mobp*, and *Plp1*), astrocytes (*Aqp4* and *Gja1*), and microglia (*Tgfbr1*). Note the presence of a subset of uncorrelated transcripts, including canonical markers of microglia cells (*Trem2*, *Irf8*, *Fcgr2b*, and *Cd68*), at the Sup sublayer in epileptic rats (red). MLE, maximum-likelihood estimate.

(D) MA plots showing epilepsy-associated significantly upregulated (red) and downregulated (blue) genes in deep and Sup CA1 sublayers (FC > 0.5, adj. $p < 0.01$) (left). Venn diagrams show the overlap of upregulated (top) and downregulated (bottom) genes between epileptic and control in Sup and deep sublayers of CA1.

(E) GO analysis of the top 250 upregulated and downregulated genes in deep and Sup sublayers in epilepsy (adj. $p < 0.1$ and then ranked by FC).

sublayer (adj. $p < 0.05$). Strikingly, significantly upregulated transcripts in the superficial sublayer of epileptic CA1 show a strong functional association with immune and inflammatory responses, including cytokine production, cell migration, cell proliferation, and programmed cell death (e.g., *Tlr3*, *Tlr7*, *C1qa*, *Csf1r*, *Tgfb1*, *Cd74*, *Cd86*, *Itgax*, *Itgam*, *Itgb2*, *Casp1*, *Casp4*, *Nlrc4*, *Pycard*, and *Tnfrsf1b*) (Figure 2E). Upregulated genes in the superficial CA1 sublayer of epileptic animals include core components of the inflammasome, such as *Nlrc4*, *Casp1*, and *Casp4*, which, upon activation, can promote pyroptosis, a pro-inflammatory form of lytic cell death (McKenzie et al., 2020). The transcript levels of the cysteine protease *Casp3*, a central effector of apoptosis, was also found to be upregulated specifically in the epileptic CA1 (global effect, adj. $p < 0.05$; superficial, adj. $p = 0.0612$; deep, adj. $p = 0.6443$). Thus, differential gene expression analysis suggests that the nature and severity of transcriptional responses to TLE may segregate radially across CA1.

Cell type deconvolution of LCM RNA-seq data suggests sublayer-specific neurodegeneration associated with microglia

Given the sublayer heterogeneity of biological processes revealed by bulk-tissue LCM RNA-seq, we reasoned that they might reflect different contributions by discrete cellular populations within the CA1 sample and/or changes in cell type composition in response to epilepsy.

To address this point, we reanalyzed a published dataset of single-cell RNA-seq (scRNA-seq) from 3,005 barcoded individual cells from the mouse somatosensory S1 cortex and CA1 regions (Zeisel et al., 2015; Figure S2I). We first performed unsupervised consensus clustering to identify major cell types in CA1 and canonical marker genes (Figures S2J and S2K). Next, to identify cell-type-specific gene signatures in bulk tissue RNA-seq data, we used scRNA-seq expression levels for the top 250 DEGs between CA1 sublayers of control and epileptic rats to summarize the cells by linear dimensionality reduction with principal-component analysis (Figure 3A). In addition, we also performed pairwise correlations and hierarchical clustering for these gene sets (Figure 3A). In control animals, these analyses revealed that gene signatures of distinct cell types, including pyramidal neurons, astrocytes, and oligodendrocytes, were prominent in the CA1 deep layer, whereas genes enriched in the superficial sublayer were mostly associated with pyramidal neurons and interneurons. In sharp contrast, we noticed strong upregulation of a core gene signature that included many known microglial markers (Micro; e.g., *Tyrobp*, *Trem2*, *Irf8*, *Irf5*, *Fcgr2b*, *Cd74*, *Cd68*, *Itgam*, and *Arpc1b*) and was specific to the superficial layer of the epileptic CA1 (Figures 3A and 3C). We further confirmed these findings using a different scRNA-seq dataset from the Allen Brain Map portal

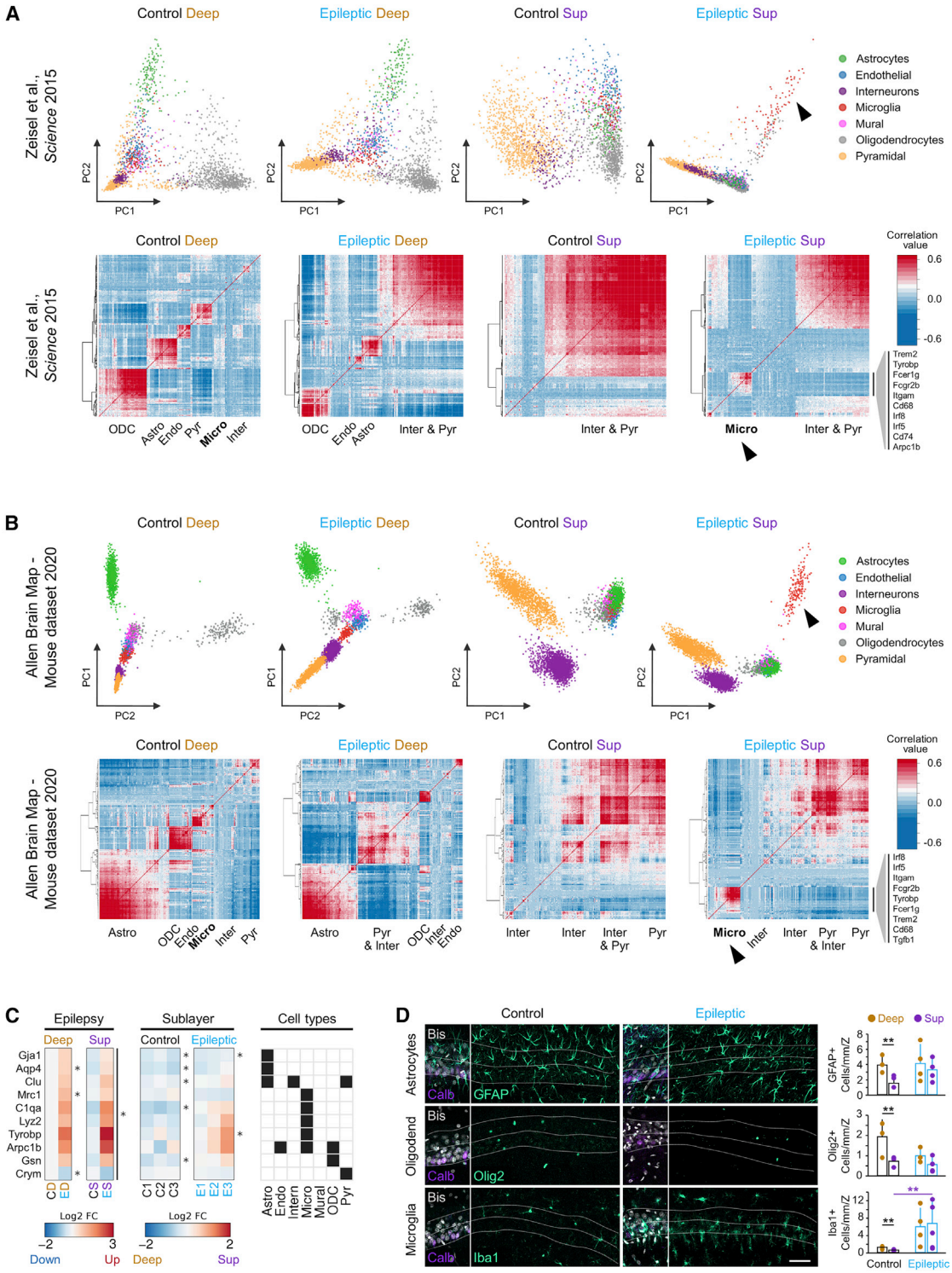

Figure 3. Microglia subpopulations underlie the transcriptional signature of Sup CA1 in epilepsy

(A and B) Subpopulation signatures inferred by deconvolution of bulk tissue transcriptome profiles. Gene sets were the top 250 DEGs between Sup and deep CA1 sublayers in epileptic and control rats (as indicated) identified in bulk tissue RNA-seq. For the selected genes, normalized expression was retrieved from publicly available scRNA-seq data from the mouse CA1 hippocampal region (Zeisel et al., 2015) (A) or the Allen Brain Map portal (Mouse Whole Cortex and Hippocampus SMART-seq [2019] with 10x-SMART-seq taxonomy [2020]) (B), and single cells were summarized by linear dimensionality reduction using principal-component

(legend continued on next page)

(Mouse Whole Cortex and Hippocampus SMART-seq [2019]) with 10x-SMART-seq taxonomy (2020) (Figure 3B). To evaluate this *in situ*, we performed immunofluorescence staining against protein markers for microglia (Iba1), astrocytes (glial fibrillary acidic protein [GFAP]), and oligodendrocytes (Olig2) and quantified their density across sublayers (Figure 3D, left). We confirmed the presence of physiological segregation of glial cell types across the CA1 sublayers (control) and changes in TLE, with between-groups differences reaching significance for microglia (Figure 3D, right).

Prompted by these results, we dissected the contribution of microglia-associated transcripts in our sample. We noticed that most of the uncorrelated transcripts in the comparison of sublayer-enriched genes across conditions were highly expressed in microglia (red dots in Figures 2C and S2F; see microglia-specific genes in Figure S2G). Thus, we evaluated their potential functional effect by building the microglial sensome (Hickman et al., 2013), which was upregulated profoundly in the superficial sublayer of epileptic rats (Figure S3A). Moreover, evaluation of microglia-neuron interactions via ligand-receptor pairing confirmed sublayer-specific effects (Figure S3B). For example, in the epileptic superficial CA1 subfield, we found dysregulated expression of the transcript encoding the CD200 receptor, whose expression in neurons provides a "don't eat me" signal that reduces microglial activation (Hoek et al., 2000). Similarly, *Cx3cl1*, a neuronal chemokine that dampens the microglia inflammatory response and neurotoxicity, was also strongly downregulated, whereas *C3* and *Csf1* transcripts were upregulated in the superficial CA1 sublayer (Biber et al., 2007; Luo et al., 2013). In contrast, the epileptic deep CA1 sublayer showed a much weaker microglia signature, and only *Cx3cl1* was found to be downregulated (Figure S3B).

Our analyses reveal heterogeneous distribution of resident cell types across the CA1 radial axis of the normal hippocampus. Strikingly, we identified critical changes in the epileptic hippocampus, including local accumulation of reactive microglia and changes of key modulators of the neuronal immune response specifically at the superficial sublayer.

CA1 hippocampal sclerosis is degenerative and sublayer specific

Given the results described above, we sought to evaluate the anatomical landscape of CA1 hippocampal sclerosis. Previously, we reported a significant reduction of linear cell density concentrated at the CA1 region in the systemic kainate model of TLE in rats, more consistent with sclerosis type 2 (Inostroza et al., 2011). To precisely evaluate CA1 sublayers, we combined immunostaining against the CA1 marker Wfs1 with the superficial marker Calbindin (Figure 4A). Proximal, intermediate, and distal CA1 segments were evaluated separately in tissue from 10 control and 10 epileptic rats (1 section per animal from −3.2 to −4.8 mm from the bregma). To avoid effects of hippocampal atrophy over cell density per area, we chose to evaluate the linear density of cells along the *stratum pyramidale* (SP) (cells per millimeter).

Cell loss in all three segments was mostly restricted to Calb+ superficial CA1 pyramidal cells in chronically epileptic rats (Figure 4B; 3-way ANOVA for group, sublayer, and proximodistal effects, all significant at $p < 0.0001$; post hoc Tukey test, $p < 0.001$). Because Calbindin immunoreactivity may be affected during epileptogenesis (You et al., 2017), we exploited the transgenic mouse line Thy1.2-G-CaMP7-DsRed2 with restricted expression on deep pyramidal cells (Figure 4C). Using this line, we estimated superficial cells as Wfs1+/DsRed2− and deep cells as Wfs1+/DsRed2+. Estimated global error by off-target Calb+/DsRed2+ expression was at 12% (10% proximal, 10% intermediate, 16% distal). We found similar regionalization of neuronal loss at the intermediate and distal segments of chronic epileptic mice using co-localization between DsRed2 and Wfs1 (Figure 4D, left; n = 3 control, n = 5 epileptic; 6–8 weeks post-status; significant interaction between group and sublayer, $p = 0.0006$; post hoc t test, $p < 0.01$).

Given a potential interaction between expression of Calbindin and aging (Iacopino and Christakos, 1990), we evaluated temporal trends of CA1 cell loss in epileptic rats, where a time-dependent decrease of Calb+ cells was appreciated ($r = -0.52$, $p = 0.097$, Pearson correlation), but not for control animals ($p = 0.66$; Figure 4E). We also examined the sublayer-specific vulnerability of CA1 neurons in the lithium-pilocarpine model in rats (Curia et al., 2008), which is more consistent with type 1 hippocampal sclerosis (Inostroza et al., 2011). Notably, pilocarpine-treated rats showed a similar reduction of Calb+ CA1 pyramidal cells early along epileptogenesis ($p = 0.0003$, n = 5 rats, 2–13 weeks post-status; Figure 4E, note full cell loss after 10 weeks post-status, arrowhead). Finally, to fully exclude an interaction with Calbindin immunoreactivity, we evaluated Wfs1+ cell density at deep and superficial sublayers by relying only on anatomical criteria (location within the sublayer) and found consistent

analysis (PCA) (top panels). Cells are colored by population membership (STAR Methods). Also shown are heatmaps of pairwise correlation for selected gene sets using scRNA-seq data, as indicated above (bottom panels). *Bona fide* markers of distinct cell types were detected in clusters of highly correlated genes representing cell type gene signatures convoluted in the bulk tissue RNA-seq (Pyr, pyramidal cell; Inter, interneuron; ODC, oligodendrocytes; Astro, astrocytes; Endo, endothelial cells; Micro, microglia; Mural, mural cells). Gene signatures of different types of cells (e.g., Pyrs, Astros, and ODCs) in the deep CA1 sublayer of control and epileptic rats lead to segregation of the cells in the corresponding PCAs and heatmap of the pairwise correlation matrix. Note the radial distribution of distinct cell types in the CA1 region in control and epileptic rats. Also note the presence of a strong gene signature of Micros in the Sup CA1 sublayer of epileptic rats (arrowhead). Names of highly correlated genes enriched in Micros are shown (Zeisel et al., 2018).

(C) Heatmaps of significantly differentially expressed cell marker genes (Figures S2I–S2K) in epilepsy in the deep or Sup sublayer (left panels), heatmap showing the sublayer effect in control and epileptic groups (paired design) for cell-marker genes modulated in epilepsy (center panels), and cell types associated with each marker gene (right panel). Pyr, pyramidal cells. *adj. $p < 0.1$.

(D) Representative sections of control and epileptic rats immunostained against GFAP (Astros), Olig2 (ODCs), and Iba1 (Micros) (left panels). The leftmost section for each condition shows co-localization between the cell type marker (cyan), Calb (purple), and bisbenzimide (Bis; white). Bar plots show quantification of astrocyte (GFAP+), ODC (Olig2+), and Micro (Iba1+) linear cell density across sublayers and groups. Shown are significant differences in interaction between sublayer and groups for Astros ($F(1,5) = 10.1$, $p = 0.022$) and Micros ($F(1,5) = 7.4$, $p = 0.042$) with post hoc differences at deep and Sup layers in the control group, the effect of the sublayer for ODCs ($F(1,5) = 23.8$, $p = 0.0045$), and differences between groups only for Micro cells. Data are from 3 control and 4 epileptic rats. *$p < 0.05$, **$p < 0.01$, post hoc tests. Scale bar, 60 μm.

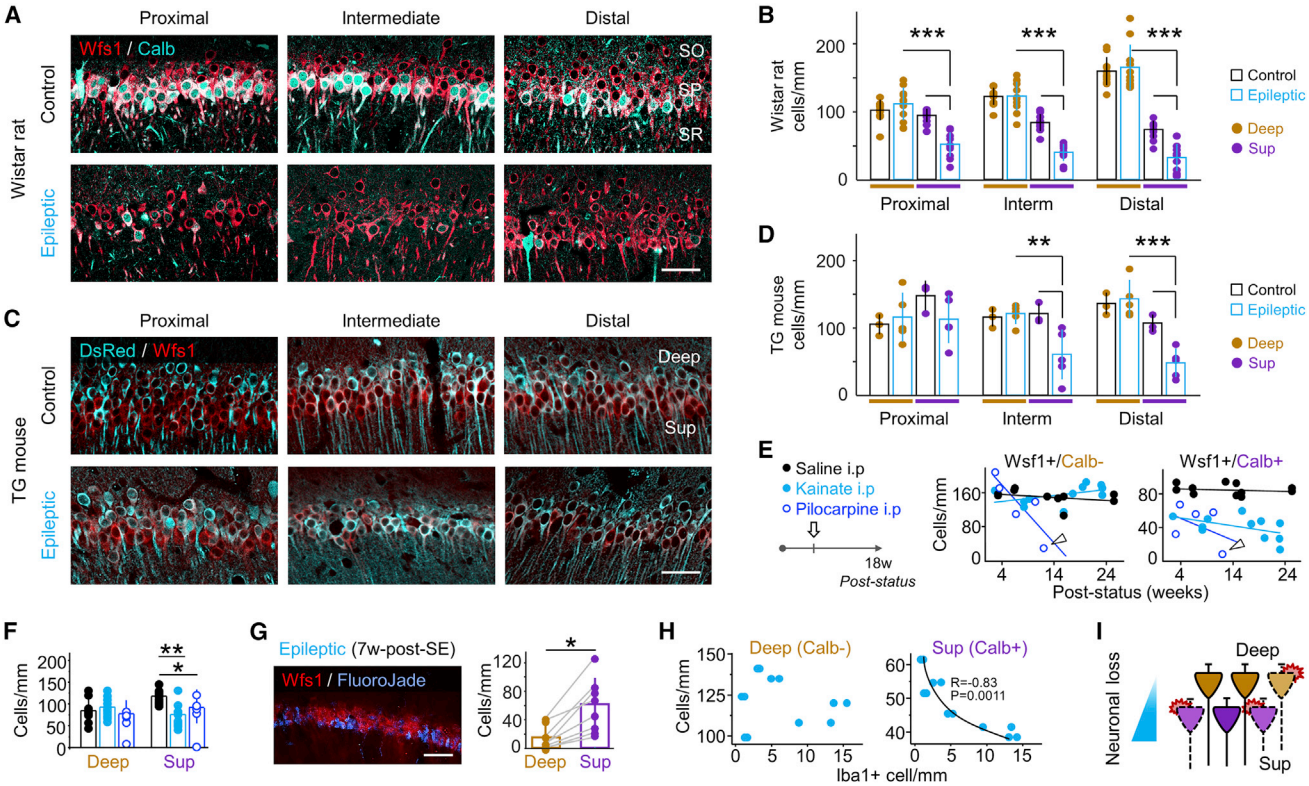

Figure 4. Hippocampal sclerosis is sublayer and cell type specific

(A) Immunostaining against the CA1 marker Wfs1 co-localized with Calb at proximal, intermediate, and distal segments in control and epileptic rats. Scale bar, 50 μm.

(B) CA1 linear cell density confirmed neuronal loss affecting mainly Calb+ cells. Data are from 10 control and 10 kainate-treated epileptic rats (1 section per rat, −3.2 to −4.8 mm from the bregma, 20×). Significant 3-way ANOVA for group ($F_{1,120} = 32.6$, $p < 0.0001$; proximodistal ($F_{2,120} = 11.7$, $p < 0.0001$) and sublayer ($F_{1,120} = 424,1$; $p < 0.0001$). Post hoc Tukey test: **$p < 0.01$, ***$p < 0.005$. Scale bar, 50 μm.

(C) Hippocampal sections from representative control and epileptic transgenic (TG) mice expressing G-GaMP7-DsRed2 in Calb− deep Pyrs.

(D) Linear density data from 3 control and 5 epileptic TG mice (1 section per mouse at 20×). Significant 3-way ANOVA for groups ($F_{1,36} = 7.8$, $p = 0.008$) and sublayers ($F_{1,36} = 8.9$, $p = 0.0051$), no proximodistal effect. Post hoc t test: **$p < 0.01$, ***$p < 0.005$.

(E) Left: experimental timeline. Right: mean density of Calb+ and Calb− CA1 Pyrs as a function of time fitted by linear trends. Data are from 10 control, 10 epileptic (kainate), and 5 epileptic (lithium-pilocarpine) rats. Arrowheads point to a lithium-pilocarpine rat with full cell loss in CA1 10 weeks after status.

(F) CA1 mean cell loss in rats quantified as deep versus Sup using Wfs1. Sup CA1 cells are more affected than deep cells. Significant effect for group in a 2-way ANOVA, $F_{2,48} = 5.9$, $p = 0.005$. Post hoc unpaired t test: *$p < 0.01$, **$p < 0.01$.

(G) Fluoro-Jade signal co-localized with Wfs1 and quantification of Fluoro-Jade+ cells across sublayers; n = 8 epileptic rats. Paired t test, *$p < 0.01$. Scale bar, 40 μm.

(H) Density of deep (Calb−, left) and Sup (Calb+, right) Pyrs against the density of Micros (Iba1+) counted at deep and Sup sublayers (data are from 6 epileptic rats). Significant Spearman decreasing monotonic trend only for Sup cells ($r = −0.87$, $p = 0.0236$).

(I) Schematic of epilepsy-associated histopathological findings indicating larger neuronal loss (blue ramp) and increased Micro cells (red) in the Sup sublayer.

results in both TLE models (Figure 4F; 2-way ANOVA for group, $p = 0.005$).

To further confirm sublayer-specific neurodegeneration, we combined Fluoro-Jade staining, which characteristically labels degenerating cells, with Wfs1 immunostaining in sections from epileptic rats (n = 8 epileptic rats) and again observed stronger neurodegeneration in superficial sublayers (Figure 4G; paired t test, $p = 0.0017$). Notably, double immunostaining against Calb and the microglial marker Iba1 revealed an inverse correlation of the amount of microglia and the density of superficial pyramidal neurons, consistent with a decreasing monotonic trend (Calb+; $r = −0.87$, $p = 0.0236$; Spearman correlation but not for deep cells [Calb−]; Figure 4H). This result indicates that loss of superficial pyramidal neurons is strongly associated with local accumulation of microglia.

Our results support the idea that hippocampal sclerosis results from specific interactions between different cell types in a particular niche (i.e., superficial CA1 pyramidal cells and activated microglia), leading to regionalized neurodegenerative signatures in the sclerotic CA1 (Figure 4I).

Single-nucleus RNA-seq confirms cell-type-specific neurodegeneration of CA1 pyramidal cells

To gain more insights into the transcriptional activity patterns underlying hippocampal sclerosis, we performed unbiased high-throughput RNA-seq of isolated single-nucleus RNA-seq

(snRNA-seq) (Figure 5A). We analyzed the transcriptomes of 6,739 single high-quality CA1 barcoded nuclei derived from 2 control and 2 epileptic mice (control, 3,661 nuclei; epilepsy, 3,078 nuclei). Consistent with recent reports (Habib et al., 2016; Zeisel et al., 2015), barcoded nuclei were automatically classified into 13 clusters, which were then aggregated into six major cell classes: excitatory neurons, interneurons, oligodendrocytes, microglia, oligodendrocyte precursor cells, and astrocytes (Figures S4A and S4B; see Figure S4C for control versus epileptic and Figure S4D for unique molecular identifier (UMI) levels and number of genes per cell type; Table S3).

We focused on pyramidal CA1 neurons, which represented 80% of the cell population (5,347 nuclei: 2,934 control and 2,413 epileptic). After two clustering rounds (Figure S4E), we identified deep and superficial pyramidal cells from control (1,123 deep, 1,810 superficial) and epileptic (878 deep and 1,469 superficial) samples and a small population of pyramidal nuclei that were mostly epilepsy-specific (Pyr_ES; 67 nuclei: 66 from epileptic CA1, 1 from control CA1) (Figure 5B). Notably, clustering exhibited consistent distribution of markers for deep (e.g., *Ndst4* and *Col11a1*) and superficial pyramidal neurons (e.g., *Calb1* and *Epha3*) (Figures S4F and S4G). The specific population of Pyr_ES cells showed total UMI values well above the quality threshold (>500 UMIs) and a number of annotated genes lying within the control and epileptic ranges (Figure S4H), excluding potential artifacts. Differential expression analysis of Pyr_ES cells against all detected cells, excluding deep and superficial pyramidal neurons, revealed enrichment of pyramidal CA1 marker genes such as *Gria2*, *Rasgrf1*, *Camkv*, and *Brd9*, along with other transcripts enriched in excitatory neurons, including *Epha6*, *Hs6st3*, *Cntnap2*, *Kcnh7*, *Kcnip4*, and *Meg3*, which confirmed their pyramidal nature (Figures S4I and S4J). Similar to our LCM RNA-seq observations at the tissue level, we found consistent correlation of sublayer-specific genes in control and epileptic samples (Figures 5C, 5D, S5).

Next, we sought to identify gene programs underlying the differential vulnerability of deep and superficial CA1 pyramidal cell in response to epilepsy (adj. $p < 0.05$). Although statistical evidence of this analysis is limited by the small sample size, it provided useful prospective hypotheses and identified many epilepsy-related transcriptional changes. Many transcripts common to both cell types were associated with modulation of synaptic transmission, synapse organization, and regulation of membrane potential (Figures 5E and 5F, common genes in black). Single-nucleus differential expression analysis also revealed striking differences between superficial and deep cells of genes involved in synaptic signaling and ion membrane transport (Figures 5E and 5F). To exclude effects of different sample sizes between groups and cell types, we evaluated the top-ranked 300 DEGs and found similar GO families to be involved differentially (Figure S6A). Deregulated genes in superficial cells in epilepsy showed a strong functional association that was related to the gamma-aminobutyric acid (GABA) signaling pathway, calcium ion transport, potassium ion transport, regulation of glutamatergic synaptic transmission, axon growth and guidance, and synapse assembly. We also noted cell-type-specific changes in genes related to neuronal survival. For instance, we found significant upregulation of death-associated protein kinase 1 (*Dapk1*) specifically in superficial CA1 neurons (Bialik and Kimchi, 2006; Figure 5G). Conversely, genes associated with the pro-survival receptors TrkB (*Ntrk2*) and TrkC (*Ntrk3*) and sortilin-related VPS10 domain-containing receptor 3 (*Sorcs3*) were upregulated exclusively in deep cells (Huang and Reichardt, 2001; Pfisterer and Khodosevich, 2017; Figure S6B). Other genes regulating neuronal vulnerability to insults were found to be deregulated in both populations of CA1 pyramidal neurons. These include the anti-apoptotic genes *Akt3*, *Chl1*, and *Spag5* and the pro-apoptotic gene *Nkain2* (He et al., 2020; Katic et al., 2017; Tawarayama et al., 2018; Figures 5G and S6B).

For some transcripts, we noted significant differential expression in epilepsy-specific Pyr_ES cells and chose to focus on this small cluster (Figure 5B, green). Compared with control pyramidal cells, Pyr_ES cells showed transcriptional dysregulation of the GO families that were altered in superficial and deep CA1 neurons in epilepsy (Figure S6C). To avoid confounding effects caused by the small sample size, we focused on transcripts identified as differentially expressed between Pyr_ES and all other epileptic cells that were well represented in both populations (i.e., detected in at least 50% of cells per group; pct.1 > 0.5 and pct.2 > 0.5 over test result). Notably, many of these transcripts were upregulated more in Pyr_ES neurons compared with other epileptic cells, including the previously mentioned apoptotic-related genes *Spag5*, *Chl1*, and *NKain2* (Figures 5G, 5H, and S6B).

To validate these findings at the single-cell level *in situ*, we used specific RNA-based probes (RNAscope) for sublayer-specific (*Dcc*) and group-specific (*Dapk1* and *Spag5*) transcripts in combination with Wfs1 immunostaining to label CA1 pyramidal cells in coronal brain sections of control and epileptic mice (n = 5 control, n = 5 epileptic mice). As expected, we observed fluorescence-labeled spots restricted to the somata of CA1 pyramidal neurons (Figures 5I, 5J, S6D, and S6E). Quantification of RNAscope revealed sublayer effects of *Dcc* (2-way ANOVA $F(1,8) = 21.59$, $p = 0.0017$) with significant post hoc differences between layers in both groups ($p < 0.05$; see also distribution per cells in Figure 5K, small dots). In contrast, for *Dapk1* ($F(1,8) = 12.99$, $p = 0.0069$) and *Spag5* ($F(1,8) = 10.53$, $p = 0.0118$), we found that significant differences between groups involved mainly the superficial sublayer, in line with our snRNA-seq results (Figure 5K).

Our analysis confirmed profound transcriptional changes related to neuronal excitability and neurodegeneration in epileptic CA1 pyramidal neurons. These functions appear to be segregated across deep and superficial cell types, consistent with electrophysiological, LCM RNA-seq, and histological data. Notably, snRNA-seq analysis revealed disease-associated genes that were highly cell type specific, including some with key functions in neuronal survival. Hence, epilepsy-induced cell-type-specific regulation of genes with key roles in synaptic plasticity and survival is a potential molecular link between differential activity burden and vulnerability across the CA1 radial axis, leading to regionalized hippocampal sclerosis.

CellPress
OPEN ACCESS

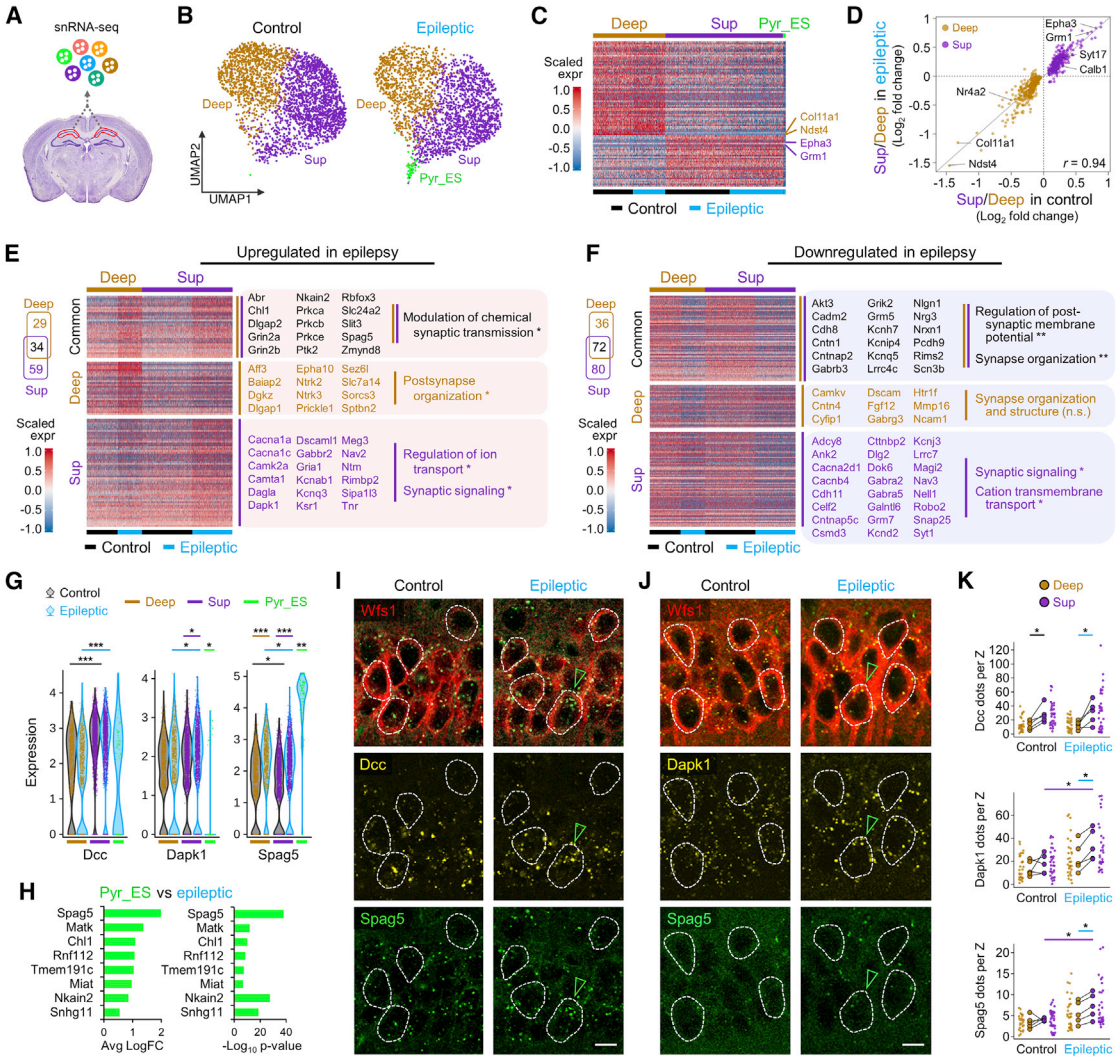

Figure 5. snRNA-seq profiling of the normal and epileptic CA1 area

(A) Nuclei were isolated from the CA1 region of adult mice and purified by flow cytometry for single-nucleus RNA-seq (snRNA-seq).

(B) Uniform manifold approximation and projection (UMAP) plots of CA1 Pyrs subtypes segregated by condition (control and epileptic). Pyr_ES, epilepsy specific.

(C) Heatmap showing normalized expression for principal gene markers for deep and Sup neurons in control and epileptic mice (96 enriched genes: 62 deep, 34 Sup; absolute log FC > 0.25; min.pct = 0.5; adj. $p < 10^{-30}$). Note the presence of a subset of cells with differential gene expression corresponding to the Pyr_ES cell population (green).

(D) Significantly enriched genes in Sup and deep CA1 neurons in control mice and their relative level of enrichment in epileptic animals (adj. $p < 0.05$, 493 genes). Gene expression levels of CA1 neuronal subtype-specific enriched genes are preserved in epilepsy.

(E) Venn diagram and heatmap of DEGs upregulated in epilepsy (adj. $p < 0.05$, Wilcoxon rank sum test). The heatmap shows normalized expression levels for upregulated DEGs that are common (34 genes), specific to deep (29 genes), or Sup (59 genes) CA1 neurons. Representative genes and associated significant GO terms are shown. FDR *adj. $p < 0.05$ (Fisher's exact test).

(F) Same as in (E) for downregulated genes.

(G) Violin plot of normalized expression value for selected genes in deep and Sup neurons in epilepsy (blue) and control (black). Wilcoxon rank-sum test; *$p < 0.05$, **$p < 10^{-10}$, ***$p < 10^{-50}$, #$p < 10^{-100}$. Expression levels in Pyr_ES cells are also shown (green).

(H) FC (left) and significance (right) for most upregulated genes in Pyr_ES compared with epileptic CA1 Pyrs (absolute log FC > 0.5 and min.pct = 0.5).

(I) Immunostaining against the CA1 marker Wfs1 and multiplexed RNAscope for *Dcc* and *Spag5* transcripts. Cells with their somata in the confocal plane are outlined. Note significant accumulation of *Spag5* in an epileptic cell (green arrowhead). Scale bar, 10 μm.

(J) Same as in (I) for *Dapk1* and *Spag5* transcripts.

(K) Quantification of *Dcc*, *Dapk1*, and *Spag5* per cell (small dots) and mouse (5 control and 5 epileptic); post hoc paired t tests, *$p < 0.05$.

Pseudotemporal ordering reveals sublayer-specific neurodegenerative progression

Based on the data above, we speculated that epilepsy-related responses and degenerative signals might evolve distinctly across cell types and sublayers. This may be especially critical for cell death programs accompanying hippocampal sclerosis. To glean insights into these transitional states, we used manifold learning leveraged in nearest-neighbor information to automatically organize cells in trajectories along a principal tree, reflecting progression of associated biological processes (Qiu et al., 2017a).

Low dimensional embedding of the automatically learned underlying trajectory produced a spanning tree, revealing a topological structure with four main branches (A, B, D, and E) and two bifurcation points (1 and 2; Figure 6A). Most nuclei at branches A and B were from cells identified as deep, whereas branches D and E were populated mostly by superficial cells (Figure 6B). Interestingly, control and epileptic cells were distributed differently. Branches A and D were mostly populated by control pyramidal cells, whereas branches B and E contained the vast majority of epileptic cells (Figures 6C and 6D). The trajectory topology suggested that the transcriptional state of single cells progresses along sublayer-specific disease trajectories from a basal state (branches A and D) to the epileptic condition (branches B and E) (Figure 6C). Notably, epilepsy-specific Pyr_ES cells were retrieved at the end of the superficial epileptic E path, suggesting that they may be superficial neurons at a terminal pathological state (Figure 6B, green arrowhead).

To identify mechanisms underlying single-cell transcriptional changes from health to disease, we performed quantitative comparison of gene expression kinetics across trajectories in each cellular population (DDRTree method) (Qiu et al., 2017b). By comparing the top-ranked 250 DEGs in deep (maximum false discovery rate [FDR] adj. $p = 8.94 \times 10^{-4}$, likelihood ratio test) versus superficial cells (maximum FDR adj. $p = 5.8 \times 10^{-19}$), we found about 50% of genes (124 genes) associated with epilepsy carrying significant cell-type-specific trajectories. Consistent with our previous results, we found that genes deregulated in epilepsy in superficial CA1 neurons show tight functional association among them, leading to a high proportion of significantly enriched ontology terms compared with genes deregulated in deep CA1 neurons (Figures 6E and 6F). Again, significantly enriched GO terms were related to structural and functional neuronal plasticity. Interestingly, pseudotemporal kinetics also revealed marked differences in the progression across sublayers of genes with important functions in regulating neuronal survival. For instance, the gene transcript levels of *Dapk1* showed a robust increase in superficial epileptic cells, whereas the gene expression levels of the pro-survival receptors TrkB (*Ntrk2*) and TrkB (*Ntrk3*), along with other genes with key functions in neurons, such as *Sorcs3* and *Aff3*, were upregulated specifically in deep pyramidal cells (Figures 6G and S6F). Other genes also related to neuronal vulnerability, such as *Camk2a* and *Nrg3*, displayed similar changes along the disease trajectory in both cell types (Figures 6G and S6F). Strikingly, the subset of apoptosis-related genes *Spag5*, *Matk*, and *Chl1* reached their maximal expression level in Pyr_ES at the end of the transcriptional trajectory in superficial cells (Figures 6G, 6H, and S6F, green).

DISCUSSION

Our work identifies sublayer-specific transcriptional changes in experimental hippocampal sclerosis. Using a combination of techniques, we found that acquired TLE involves heterogeneous biological processes running across deep and superficial CA1 pyramidal cells. Our data suggest that epileptogenesis and the accompanying hippocampal sclerosis are evolving processes that affect the transcriptional state of neurons in a cell-type-specific manner.

Hippocampal sclerosis is a heterogeneous histopathological entity (Blümcke et al., 2013). The prognosis value of certain subtypes has been debated, but emerging data suggest that it deserves further consideration in light of cell type specificity (Prada Jardim et al., 2018). Superficial and deep CA1 pyramidal cells are innervated differently by local-circuit GABAergic interneurons, express different neuromodulatory receptors, project differentially to cortical and subcortical regions, and participate distinctly in hippocampal oscillations (Cembrowski et al., 2016a; Soltesz and Losonczy, 2018; Valero and de la Prida, 2018). The more sustained excitability of superficial pyramidal cells (in terms of post-event depolarization and increased firing rate) and their consistent stronger expression of the immediate-early gene-associated protein c-Fos after individual seizures suggest that they have a larger activity burden compared with deep cells (Figure 1). Although our snRNA-seq analysis identified many transcripts regulated differentially between deep and superficial CA1 neurons that may underlie pro-epileptogenic changes in intrinsic excitability, microcircuit mechanisms are key contributors to these differences. First, perisomatic inhibition by parvalbumin (PV) basket cells is remarkably higher in deep compared with superficial cells (Soltesz and Losonczy, 2018; Valero et al., 2015). Second, superficial cells are more likely to be driven by presynaptic CA3 activity than deep cells (Valero et al., 2015). Similarly, direct inputs from layer III pyramidal neurons in the medial entorhinal cortex are biased by deep CA1 cells, whereas projections from the lateral entorhinal cortex are stronger in superficial cells (Masurkar et al., 2017). Given loss of medial layer III inputs and sprouting of lateral inputs together with specific cannabinoid type 1 receptors pathways (Laurent et al., 2015; Maroso et al., 2016), it is very likely that these changes contribute to more sustained activation of superficial cells in the epilepsy context.

Transcriptional dysregulation is a central feature of most neurodegenerative diseases. Our transcriptional profiling in laser-microdissected CA1 deep and superficial sublayers (LCM RNA-seq) revealed strong regionalized responses to acquired epilepsy. We found significantly larger transcriptional changes of GO terms associated with immune and inflammatory processes, cytokine production, and programmed cell death in the superficial sublayer (Figure 2). This includes *Cx3cr1*, *P2ry12*, and *Il18*, among other genes described previously, playing major roles in microglial activation and neurodegeneration associated with epilepsy (Ali et al., 2015; Eyo et al., 2014; Vezzani and Baram, 2007). For the deep pyramidal sublayer, transcriptional changes were milder in general and mostly involved deregulation of genes associated with changes in excitability, homeostatic regulation, and synaptic signaling, such as *Kcnh7*, *Kcnip4*,

CellPress
OPEN ACCESS

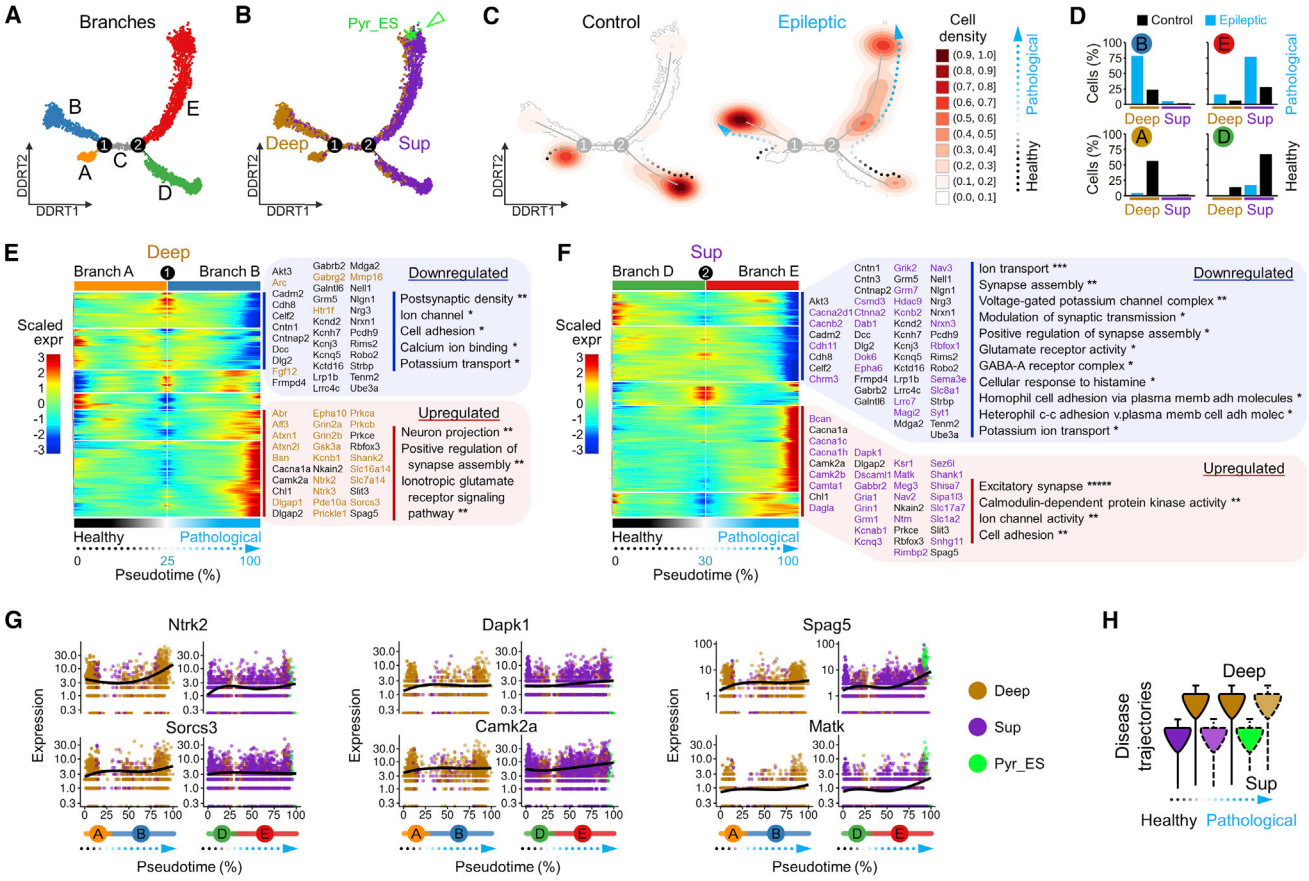

Figure 6. Pseudotemporal ordering of transcriptional changes unfolds separate disease trajectories across CA1 sublayers

(A) UMAP plot of pseudotemporal trajectory analysis of Pyr subpopulations along with discriminative dimensionality reduction via learning a tree(DDRTree) coordinates uncovers four major branches (A, B, D, and E) and segregated from two branchpoints (1 and 2).

(B) Distribution of Pyr subpopulations (deep, Sup, and Pyr_ES) across pseudotime trajectories. An arrowhead points to Pyr_ES cells located at the endpoint of branch E.

(C) Distribution of Pyr subpopulations across pseudotime trajectories by condition (control and epileptic).

(D) Distribution of Pyr subtypes across the trajectory topology.

(E) Heatmap of the top-ranked branched expression analysis modeling (BEAM) significant changes through progression across the trajectory from branch A (basal state) to B (epilepsy) (deep cells). Each row indicates the standardized kinetic curves of a gene.

(F) Same as (E) for the Sup-specific trajectory from basal state (branch D) to the epileptic condition (branch E).

(G) Pseudotime kinetics across disease trajectory for selected DEGs in epilepsy.

(H) Schematic of disease trajectories from control to epilepsy.

Scn3b, and *Gabrb3* (Dixit et al., 2016; Steinlein and Noebels, 2000). Many of these changes were confirmed by snRNA-seq analysis (Figure 5), which disclosed significant upregulation of the *Dapk1* specifically in superficial CA1 neurons (Bialik and Kimchi, 2006), whereas genes associated with the pro-survival receptors TrkB (*Ntrk2*) and TrkC (*Ntrk3*) and *Sorcs3* were mostly upregulated in deep cells (Huang and Reichardt, 2001; Pfisterer and Khodosevich, 2017).

By leveraging unsupervised branched expression learning, we identified deviating transcriptional disease trajectories in deep and superficial pyramidal cells (Figure 6). Some of the GO terms involved suggest that transition from the normal to the epileptic condition in deep cells is more likely associated with changes in synaptic signaling and excitability (i.e., they reflect microcircuit alterations), whereas superficial cells move differentially along transcriptional changes affecting cell-cell communication (i.e., neuron-microglia interactions). Such different latent trends might suggest that deep and superficial cells are at different stages in the neurodegenerative process or being affected by pathways leading to differential vulnerability. For instance, although we found deregulated expression of genes associated with apoptotic pathways that were common to both cell types in response to epilepsy (i.e., *Akt3*, *Nrg3*, and *Camk2a*) (Ashpole and Hudmon, 2011; He et al., 2020; Kanekura et al., 2005; Tawarayama et al., 2018; Vest et al., 2010), genes related to cell death were found to be deregulated specifically in superficial or deep neurons. In superficial cells, epilepsy resulted in decreased expression of brain-derived neurotrophic factor (*Bdnf*) and increased transcript levels of the pro-apoptotic pathway activator *Dapk1* (Bialik and Kimchi, 2006). Conversely,

in deep pyramidal neurons, epilepsy led to a robust increase in expression of the gene encoding the pro-survival receptors TrkB (*Ntrk2*) and TrkC (*Ntrk3*) (Huang and Reichardt, 2001; Pfisterer and Khodosevich, 2017). Interestingly, pseudotime analysis mapped some control cells along the epileptic branches in both sublayers, suggesting that latent sublayer-specific transcriptional processes might actually be running along life (Bishop et al., 2010).

Our snRNA-seq analysis also disclosed an epilepsy-specific pyramidal cell population, Pyr_ES, which accumulated at the end of the superficial trajectory branch (Figure 6B, arrowhead). This subset of pyramidal cells displayed remarkable expression of neurodegeneration-related transcripts such as *Cdk5*, *Ckb*, *Matk*, *Chl1*, and *Spag5* (Patrick et al., 1999). The presence of cells with very high numbers of *Spag5* molecules in the superficial sublayer of the epileptic CA1 was confirmed by combined immunofluorescence and single-molecule amplification methods. Our results indicate that genes dysregulated more in epilepsy are expressed specifically by a vulnerable subset of pyramidal neurons undergoing later stages of neurodegeneration by the time of sampling. We propose that Pyr_ES cells reflect the accumulated pro-epileptic transitional changes leading to epileptogenesis and neurodegeneration, as suggested by their extreme location along disease trajectories.

Our results identify previously unobserved heterogeneity in the neuronal patterns of activity of deep and superficial CA1 pyramidal neurons in epilepsy, show specific gene expression signatures across CA1 deep and superficial sublayers that are associated with neuronal loss and hippocampal sclerosis, reveal disease trajectories of deep and superficial CA1 pyramidal neurons in epilepsy, and uncover the underlying transcriptional programs. By dissecting the transcriptional landscape across CA1 sublayers in epilepsy, our work offers insights into the mechanisms regulating epileptogenesis and highlights the importance of leveraging cell type specificity to better understand the phenotypic complexities accompanying hippocampal sclerosis in epilepsy.

STAR★METHODS

Detailed methods are provided in the online version of this paper and include the following:

- KEY RESOURCES TABLE
- RESOURCE AVAILABILITY
  - Lead contact
  - Materials availability
  - Data and code availability
- EXPERIMENTAL MODEL AND SUBJECT DETAILS
- METHOD DETAILS
  - EEG recordings and analysis
  - *In vivo* recording and labeling of single cells
  - Analysis of intracellular single-cell recordings
  - cFos immunostaining and analysis
  - Laser capture microdissection (LCM) and RNA isolation
  - LCM RNA-seq library construction and sequencing
  - LCM RNA-seq data analysis
  - LCM RNA-seq single-cell informed data analysis
  - Single-nuclei isolation
  - Single-nucleus RNA sequencing
  - snRNA-seq analysis
  - Cell trajectories and pseudotime analysis
  - Cell-type immunostaining and analysis
  - FluoroJade staining
  - *In situ* hybridization analysis
  - RNAscope analysis
- QUANTIFICATION AND STATISTICAL ANALYSIS

SUPPLEMENTAL INFORMATION

Supplemental information can be found online at https://doi.org/10.1016/j.celrep.2021.109229.

ACKNOWLEDGMENTS

We thank Antonio Caler, Laura Dolón, Ester Lara, Beatriz Lázaro, and Juan Moriano for technical help. This work was supported by grants from MICINN (RTI2018-098581-B-I00 to L.M.P.), Fundación Tatiana Pérez de Guzman el Bueno, and the SynCogDis Network (SAF2014-52624-REDT and SAF2017-90664-REDT to L.M.P. and A. Bayes). Collaboration between L.M.d.l.P. and Y.H. was supported by Human Frontiers Science Program (HFSP) grant RGP0022/2013. J.P.L.-A. was supported by grants from MICIU co-financed by ERDF (RYC-2015-18056 and RTI2018-102260-B-I00) and Severo Ochoa grant SEV-2017-0723. R.R.-V. and A. Bayes were supported by MINECO BFU2015-69717-P and RTI2018-097037-B-100 and a Marie Curie career integration grant (ref. 304111). A.V.M. was supported by MICINN (SAF2017-85717-R) and Fundación Alicia Koplowitz. A. Barco was supported by grants SAF2017-87928-R from MICINN co-financed by ERDF and RGP0039/2017 from the Human Frontiers Science Program Organization. The Instituto de Neurociencias is a "Centre of Excellence Severo Ochoa." D.G.-D. and C.M.N. hold PhD fellowships from MICINN (BES-2013-064171 and BES-2016-076281, respectively).

AUTHOR CONTRIBUTIONS

Conceptualization, L.M.d.l.P. and J.P.L.-A.; methodology, L.M.d.l.P., J.P.L.-A., A. Bayés, and A. Barco; investigation, E.C., M.V., B.G., D.C.M., C.M.N., L.B.-E., R.R.-V., A.V.M., I.F.-L., and D.G.-D.; formal analysis, E.C., A.M.-G., M.V., J.P.L.-A., and L.M.d.l.P.; software, A.M.-G., and J.P.L.-A.; resources, Y.H., and M.S.; writing – original draft, L.M.d.l.P. and J.P.L.-A.; writing – reviewing & editing, L.M.d.l.P., J.P.L.-A., E.C., and A.M.-G.; funding acquisition, L.M.d.l.P. and J.P.L.-A.; supervision, L.M.d.l.P. and J.P.L.-A.

DECLARATION OF INTERESTS

The authors declare no competing interests.

Received: September 16, 2020
Revised: March 18, 2021
Accepted: May 17, 2021
Published: June 8, 2021

REFERENCES

Ali, I., Chugh, D., and Ekdahl, C.T. (2015). Role of fractalkine-CX3CR1 pathway in seizure-induced microglial activation, neurodegeneration, and neuroblast production in the adult rat brain. Neurobiol. Dis. *74*, 194–203.

Anders, S., Pyl, P.T., and Huber, W. (2015). HTSeq–a Python framework to work with high-throughput sequencing data. Bioinformatics *31*, 166–169.

Ashpole, N.M., and Hudmon, A. (2011). Excitotoxic neuroprotection and vulnerability with CaMKII inhibition. Mol. Cell. Neurosci. *46*, 720–730.

Benjamini, Y., and Hochberg, Y. (1995). Controlling the False Discovery Rate: A Practical and Powerful Approach to Multiple Testing. J. R. Stat. Soc. B Methodol. *57*, 289–300.

Bialik, S., and Kimchi, A. (2006). The death-associated protein kinases: structure, function, and beyond. Annu. Rev. Biochem. *75*, 189–210.

Biber, K., Neumann, H., Inoue, K., and Boddeke, H.W.G.M. (2007). Neuronal 'On' and 'Off' signals control microglia. Trends Neurosci. *30*, 596–602.

Bishop, N.A., Lu, T., and Yankner, B.A. (2010). Neural mechanisms of ageing and cognitive decline. Nature *464*, 529–535.

Blümcke, I., Kistner, I., Clusmann, H., Schramm, J., Becker, A.J., Elger, C.E., Bien, C.G., Merschhemke, M., Meencke, H.-J., Lehmann, T., et al. (2009). Towards a clinico-pathological classification of granule cell dispersion in human mesial temporal lobe epilepsies. Acta Neuropathol. *117*, 535–544.

Blümcke, I., Thom, M., Aronica, E., Armstrong, D.D., Bartolomei, F., Bernasconi, A., Bernasconi, N., Bien, C.G., Cendes, F., Coras, R., et al. (2013). International consensus classification of hippocampal sclerosis in temporal lobe epilepsy: a Task Force report from the ILAE Commission on Diagnostic Methods. Epilepsia *54*, 1315–1329.

Butler, A., Hoffman, P., Smibert, P., Papalexi, E., and Satija, R. (2018). Integrating single-cell transcriptomic data across different conditions, technologies, and species. Nat. Biotechnol. *36*, 411–420.

Cembrowski, M.S., Bachman, J.L., Wang, L., Sugino, K., Shields, B.C., and Spruston, N. (2016a). Spatial Gene-Expression Gradients Underlie Prominent Heterogeneity of CA1 Pyramidal Neurons. Neuron *89*, 351–368.

Cembrowski, M.S., Wang, L., Sugino, K., Shields, B.C., and Spruston, N. (2016b). Hipposeq: a comprehensive RNA-seq database of gene expression in hippocampal principal neurons. eLife *5*, e14997.

Chen, Z., Brodie, M.J., Liew, D., and Kwan, P. (2018). Treatment Outcomes in Patients With Newly Diagnosed Epilepsy Treated With Established and New Antiepileptic Drugs: A 30-Year Longitudinal Cohort Study. JAMA Neurol. *75*, 279–286.

Cid, E., and de la Prida, L.M. (2019). Methods for single-cell recording and labeling in vivo. J. Neurosci. Methods *325*, 108354.

Coras, R., Pauli, E., Li, J., Schwarz, M., Rössler, K., Buchfelder, M., Hamer, H., Stefan, H., and Blumcke, I. (2014). Differential influence of hippocampal subfields to memory formation: insights from patients with temporal lobe epilepsy. Brain *137*, 1945–1957.

Curia, G., Longo, D., Biagini, G., Jones, R.S.G., and Avoli, M. (2008). The pilocarpine model of temporal lobe epilepsy. J. Neurosci. Methods *172*, 143–157.

Davies, K.G., Hermann, B.P., Dohan, F.C., Jr., Foley, K.T., Bush, A.J., and Wyler, A.R. (1996). Relationship of hippocampal sclerosis to duration and age of onset of epilepsy, and childhood febrile seizures in temporal lobectomy patients. Epilepsy Res. *24*, 119–126.

de Lanerolle, N.C., Kim, J.H., Williamson, A., Spencer, S.S., Zaveri, H.P., Eid, T., and Spencer, D.D. (2003). A retrospective analysis of hippocampal pathology in human temporal lobe epilepsy: evidence for distinctive patient subcategories. Epilepsia *44*, 677–687.

Dixit, A.B., Banerjee, J., Srivastava, A., Tripathi, M., Sarkar, C., Kakkar, A., Jain, M., and Chandra, P.S. (2016). RNA-seq analysis of hippocampal tissues reveals novel candidate genes for drug refractory epilepsy in patients with MTLE-HS. Genomics *107*, 178–188.

Dobin, A., Davis, C.A., Schlesinger, F., Drenkow, J., Zaleski, C., Jha, S., Batut, P., Chaisson, M., and Gingeras, T.R. (2013). STAR: ultrafast universal RNA-seq aligner. Bioinformatics *29*, 15–21.

Dong, H.-W., Swanson, L.W., Chen, L., Fanselow, M.S., and Toga, A.W. (2009). Genomic-anatomic evidence for distinct functional domains in hippocampal field CA1. Proc. Natl. Acad. Sci. USA *106*, 11794–11799.

Du, F., Eid, T., Lothman, E.W., Köhler, C., and Schwarcz, R. (1995). Preferential neuronal loss in layer III of the medial entorhinal cortex in rat models of temporal lobe epilepsy. J. Neurosci. *15*, 6301–6313.

Eyo, U.B., Peng, J., Swiatkowski, P., Mukherjee, A., Bispo, A., and Wu, L.J. (2014). Neuronal hyperactivity recruits microglial processes via neuronal NMDA receptors and microglial P2Y12 receptors after status epilepticus. J. Neurosci. *34*, 10528–10540.

Habib, N., Li, Y., Heidenreich, M., Swiech, L., Avraham-Davidi, I., Trombetta, J.J., Hession, C., Zhang, F., and Regev, A. (2016). Div-Seq: Single-nucleus RNA-Seq reveals dynamics of rare adult newborn neurons. Science *353*, 925–928.

He, J., Green, A.R., Li, Y., Chan, S.Y.T., and Liu, D.X. (2020). SPAG5: An Emerging Oncogene. Trends Cancer *6*, 543–547.

Hickman, S.E., Kingery, N.D., Ohsumi, T.K., Borowsky, M.L., Wang, L.C., Means, T.K., and El Khoury, J. (2013). The microglial sensome revealed by direct RNA sequencing. Nat. Neurosci. *16*, 1896–1905.

Hoek, R.H., Ruuls, S.R., Murphy, C.A., Wright, G.J., Goddard, R., Zurawski, S.M., Blom, B., Homola, M.E., Streit, W.J., Brown, M.H., et al. (2000). Down-regulation of the macrophage lineage through interaction with OX2 (CD200). Science *290*, 1768–1771.

Huang, E.J., and Reichardt, L.F. (2001). Neurotrophins: roles in neuronal development and function. Annu. Rev. Neurosci. *24*, 677–736.

Huang, W., Sherman, B.T., and Lempicki, R.A. (2009). Systematic and integrative analysis of large gene lists using DAVID bioinformatics resources. Nat. Protoc. *4*, 44–57.

Huber, W., Carey, V.J., Gentleman, R., Anders, S., Carlson, M., Carvalho, B.S., Bravo, H.C., Davis, S., Gatto, L., Girke, T., et al. (2015). Orchestrating high-throughput genomic analysis with Bioconductor. Nat. Methods *12*, 115–121.

Iacopino, A.M., and Christakos, S. (1990). Specific reduction of calcium-binding protein (28-kilodalton calbindin-D) gene expression in aging and neurodegenerative diseases. Proc. Natl. Acad. Sci. USA *87*, 4078–4082.

Inostroza, M., Cid, E., Brotons-Mas, J., Gal, B., Aivar, P., Uzcategui, Y.G., Sandi, C., and Menendez de la Prida, L. (2011). Hippocampal-dependent spatial memory in the water maze is preserved in an experimental model of temporal lobe epilepsy in rats. PLoS ONE *6*, e22372.

Jefferys, J.G.R., Menendez de la Prida, L., Wendling, F., Bragin, A., Avoli, M., Timofeev, I., and Lopes da Silva, F.H. (2012). Mechanisms of physiological and epileptic HFO generation. Prog. Neurobiol. *98*, 250–264.

Kanekura, K., Hashimoto, Y., Kita, Y., Sasabe, J., Aiso, S., Nishimoto, I., and Matsuoka, M. (2005). A Rac1/phosphatidylinositol 3-kinase/Akt3 anti-apoptotic pathway, triggered by AlsinLF, the product of the ALS2 gene, antagonizes Cu/Zn-superoxide dismutase (SOD1) mutant-induced motoneuronal cell death. J. Biol. Chem. *280*, 4532–4543.

Katic, J., Loers, G., Tosic, J., Schachner, M., and Kleene, R. (2017). The cell adhesion molecule CHL1 interacts with patched-1 to regulate apoptosis during postnatal cerebellar development. J. Cell Sci. *130*, 2606–2619.

Kiselev, V.Y., Kirschner, K., Schaub, M.T., Andrews, T., Yiu, A., Chandra, T., Natarajan, K.N., Reik, W., Barahona, M., Green, A.R., and Hemberg, M. (2017). SC3: consensus clustering of single-cell RNA-seq data. Nat. Methods *14*, 483–486.

Laurent, F., Brotons-Mas, J.R., Cid, E., Lopez-Pigozzi, D., Valero, M., Gal, B., and de la Prida, L.M. (2015). Proximodistal structure of theta coordination in the dorsal hippocampus of epileptic rats. J. Neurosci. *35*, 4760–4775.

Li, H., Handsaker, B., Wysoker, A., Fennell, T., Ruan, J., Homer, N., Marth, G., Abecasis, G., and Durbin, R.; 1000 Genome Project Data Processing Subgroup (2009). The Sequence Alignment/Map format and SAMtools. Bioinformatics *25*, 2078–2079.

Liao, Y., Wang, J., Jaehnig, E.J., Shi, Z., and Zhang, B. (2019). WebGestalt 2019: gene set analysis toolkit with revamped UIs and APIs. Nucleic Acids Res. *47*, W199–W205.

Love, M.I., Huber, W., and Anders, S. (2014). Moderated estimation of fold change and dispersion for RNA-seq data with DESeq2. Genome Biol. *15*, 550.

Luo, J., Elwood, F., Britschgi, M., Villeda, S., Zhang, H., Ding, Z., Zhu, L., Alabsi, H., Getachew, R., Narasimhan, R., et al. (2013). Colony-stimulating factor 1 receptor (CSF1R) signaling in injured neurons facilitates protection and survival. J. Exp. Med. *210*, 157–172.

Maroso, M., Szabo, G.G., Kim, H.K., Alexander, A., Bui, A.D., Lee, S.-H., Lutz, B., and Soltesz, I. (2016). Cannabinoid Control of Learning and Memory through HCN Channels. Neuron *89*, 1059–1073.

Masurkar, A.V., Srinivas, K.V., Brann, D.H., Warren, R., Lowes, D.C., and Siegelbaum, S.A. (2017). Medial and Lateral Entorhinal Cortex Differentially Excite Deep versus Superficial CA1 Pyramidal Neurons. Cell Rep. *18*, 148–160.

Mathern, G.W., Kuhlman, P.A., Mendoza, D., and Pretorius, J.K. (1997). Human fascia dentata anatomy and hippocampal neuron densities differ depending on the epileptic syndrome and age at first seizure. J. Neuropathol. Exp. Neurol. *56*, 199–212.

McInnes, L., Healy, J., and Melville, J. (2018). UMAP: Uniform Manifold Approximation and Projection for Dimension Reduction. arXiv, arXiv:1802.03426. https://arxiv.org/abs/1802.03426.

McKenzie, B.A., Dixit, V.M., and Power, C. (2020). Fiery Cell Death: Pyroptosis in the Central Nervous System. Trends Neurosci. *43*, 55–73.

Morin-Brureau, M., Milior, G., Royer, J., Chali, F., Le Duigou, C., Savary, E., Blugeon, C., Jourdren, L., Akbar, D., Dupont, S., et al. (2018). Microglial phenotypes in the human epileptic temporal lobe. Brain *141*, 3343–3360.

Morris, M.E., Baimbridge, K.G., el-Beheiry, H., Obrocea, G.V., and Rosen, A.S. (1995). Correlation of anoxic neuronal responses and calbindin-D28k localization in stratum pyramidale of rat hippocampus. Hippocampus *5*, 25–39.

Patrick, G.N., Zukerberg, L., Nikolic, M., de la Monte, S., Dikkes, P., and Tsai, L.H. (1999). Conversion of p35 to p25 deregulates Cdk5 activity and promotes neurodegeneration. Nature *402*, 615–622.

Pfisterer, U., and Khodosevich, K. (2017). Neuronal survival in the brain: neuron type-specific mechanisms. Cell Death Dis. *8*, e2643.

Pfisterer, U., Petukhov, V., Demharter, S., Meichsner, J., Thompson, J.J., Batiuk, M.Y., Martinez, A.A., Vasistha, N.A., Thakur, A., Mikkelsen, J., et al. (2020). Identification of epilepsy-associated neuronal subtypes and gene expression underlying epileptogenesis. Nat. Commun. *11*, 5038.

Prada Jardim, A., Liu, J., Baber, J., Michalak, Z., Reeves, C., Ellis, M., Novy, J., de Tisi, J., McEvoy, A., Miserocchi, A., et al. (2018). Characterising subtypes of hippocampal sclerosis and reorganization: correlation with pre and postoperative memory deficit. Brain Pathol. *28*, 143–154.

Qiu, X., Mao, Q., Tang, Y., Wang, L., Chawla, R., Pliner, H.A., and Trapnell, C. (2017a). Reversed graph embedding resolves complex single-cell trajectories. Nat. Methods *14*, 979–982.

Qiu, X., Hill, A., Packer, J., Lin, D., Ma, Y.A., and Trapnell, C. (2017b). Single-cell mRNA quantification and differential analysis with Census. Nat. Methods *14*, 309–315.

Rodrigues, G.R., Kandratavicius, L., Peixoto-Santos, J.E., Monteiro, M.R., Gargaro, A.C., Geraldi, C. de V.L., Velasco, T.R., and Leite, J.P. (2015). Increased frequency of hippocampal sclerosis ILAE type 2 in patients with mesial temporal lobe epilepsy with normal episodic memory. Brain *138*, e359.

Saghafi, S., Ferguson, L., Hogue, O., Gales, J.M., Prayson, R., and Busch, R.M. (2018). Histopathologic subtype of hippocampal sclerosis and episodic memory performance before and after temporal lobectomy for epilepsy. Epilepsia *59*, 825–833.

Scandaglia, M., Lopez-Atalaya, J.P., Medrano-Fernandez, A., Lopez-Cascales, M.T., Del Blanco, B., Lipinski, M., Benito, E., Olivares, R., Iwase, S., Shi, Y., and Barco, A. (2017). Loss of Kdm5c Causes Spurious Transcription and Prevents the Fine-Tuning of Activity-Regulated Enhancers in Neurons. Cell Rep. *21*, 47–59.

Slomianka, L., Amrein, I., Knuesel, I., Sørensen, J.C., and Wolfer, D.P. (2011). Hippocampal pyramidal cells: the reemergence of cortical lamination. Brain Struct. Funct. *216*, 301–317.

Soltesz, I., and Losonczy, A. (2018). CA1 pyramidal cell diversity enabling parallel information processing in the hippocampus. Nat. Neurosci. *21*, 484–493.

Steinlein, O.K., and Noebels, J.L. (2000). Ion channels and epilepsy in man and mouse. Curr. Opin. Genet. Dev. *10*, 286–291.

Stuart, T., Butler, A., Hoffman, P., Hafemeister, C., Papalexi, E., Mauck, W.M., 3rd, Hao, Y., Stoeckius, M., Smibert, P., and Satija, R. (2019). Comprehensive Integration of Single-Cell Data. Cell *177*, 1888–1902.e21.

Tawarayama, H., Yamada, H., Amin, R., Morita-Fujimura, Y., Cooper, H.M., Shinmyo, Y., Kawata, M., Ikawa, S., and Tanaka, H. (2018). Draxin regulates hippocampal neurogenesis in the postnatal dentate gyrus by inhibiting DCC-induced apoptosis. Sci. Rep. *8*, 840.

Thom, M., Liagkouras, I., Martinian, L., Liu, J., Catarino, C.B., and Sisodiya, S.M. (2012). Variability of sclerosis along the longitudinal hippocampal axis in epilepsy: a post mortem study. Epilepsy Res. *102*, 45–59.

Thorvaldsdóttir, H., Robinson, J.T., and Mesirov, J.P. (2013). Integrative Genomics Viewer (IGV): high-performance genomics data visualization and exploration. Brief. Bioinform. *14*, 178–192.

Valero, M., and de la Prida, L.M. (2018). The hippocampus in depth: a sublayer-specific perspective of entorhinal-hippocampal function. Curr. Opin. Neurobiol. *52*, 107–114.

Valero, M., Cid, E., Averkin, R.G., Aguilar, J., Sanchez-Aguilera, A., Viney, T.J., Gomez-Dominguez, D., Bellistri, E., and de la Prida, L.M. (2015). Determinants of different deep and superficial CA1 pyramidal cell dynamics during sharp-wave ripples. Nat. Neurosci. *18*, 1281–1290.

Valero, M., Averkin, R.G., Fernandez-Lamo, I., Aguilar, J., Lopez-Pigozzi, D., Brotons-Mas, J.R., Cid, E., Tamas, G., and Menendez de la Prida, L. (2017). Mechanisms for Selective Single-Cell Reactivation during Offline Sharp-Wave Ripples and Their Distortion by Fast Ripples. Neuron *94*, 1234–1247.e7.

van der Maaten, L., and Hinton, G. (2009). Visualizing Data using t-SNE. J. Mach. Learn. Res. *9*, 2579–2605.

Vest, R.S., O'Leary, H., Coultrap, S.J., Kindy, M.S., and Bayer, K.U. (2010). Effective post-insult neuroprotection by a novel Ca(2+)/ calmodulin-dependent protein kinase II (CaMKII) inhibitor. J. Biol. Chem. *285*, 20675–20682.

Vezzani, A., and Baram, T.Z. (2007). New roles for interleukin-1 Beta in the mechanisms of epilepsy. Epilepsy Curr. *7*, 45–50.

Winden, K.D., Bragin, A., Engel, J., and Geschwind, D.H. (2015). Molecular alterations in areas generating fast ripples in an animal model of temporal lobe epilepsy. Neurobiol. Dis. *78*, 35–44.

Wittner, L., Eross, L., Szabó, Z., Tóth, S., Czirják, S., Halász, P., Freund, T.F., and Maglóczky, Z.S. (2002). Synaptic reorganization of calbindin-positive neurons in the human hippocampal CA1 region in temporal lobe epilepsy. Neuroscience *115*, 961–978.

Wyler, A.R., Curtis Dohan, F., Schweitzer, J.B., and Berry, A.D. (1992). A grading system for mesial temporal pathology (hippocampal sclerosis) from anterior temporal lobectomy. J. Epilepsy *5*, 220–225.

You, J.C., Muralidharan, K., Park, J.W., Petrof, I., Pyfer, M.S., Corbett, B.F., LaFrancois, J.J., Zheng, Y., Zhang, X., Mohila, C.A., et al. (2017). Epigenetic suppression of hippocampal calbindin-D28k by ΔFosB drives seizure-related cognitive deficits. Nat. Med. *23*, 1377–1383.

Zeisel, A., Muñoz-Manchado, A.B., Codeluppi, S., Lönnerberg, P., Manno, G., La Juréus, A., Marques, S., Munguba, H., He, L., Betsholtz, C., et al. (2015). Cell types in the mouse cortex and hippocampus revealed by single-cell RNA-seq. Science *347*, 1138–1142.

Zeisel, A., Hochgerner, H., Lönnerberg, P., Johnsson, A., Memic, F., van der Zwan, J., Häring, M., Braun, E., Borm, L.E., La Manno, G., et al. (2018). Molecular Architecture of the Mouse Nervous System. Cell *174*, 999–1014.e22.

STAR★METHODS

KEY RESOURCES TABLE

REAGENT or RESOURCE	SOURCE	IDENTIFIER
Antibodies		
Rabbit anti-calbindin D-28k	Swant	Cat# CB38; RRID: AB_10000340
Mouse anti-calbindin D-28k	Swant	Cat# 300; RRID: AB_10000347
Rabbit anti-Wfs1	Proteintech	Cat# 11558-1-AP; RRID: AB_2216046
Rabbit anti-Iba1	Wako	Cat# 019-19741; RRID: AB_839504
Rabbit anti-GFAP	Sigma	Cat# G9269; RRID: AB_477035
Rabbit anti-Olig2	Millipore	Cat# AB9610; RRID: AB_570666
Rabbit anti-cFos	Santa Cruz Biotechnology	Cat# sc-52; RRID: AB_2106783
Alexa Fluor633 goat anti-rabbit IgG	Thermo Fisher	Cat# A21070; RRID: AB_2535731
Alexa Fluor488 donkey anti-mouse IgG	Thermo Fisher	Cat# A21202; RRID: AB_141607
Alexa Fluor488 goat anti-mouse IgG	Jackson Immunoresearch	Cat# 115-545-003; RRID: AB_2338840
Rhodamine Red goat anti-mouse IgG	Jackson Immunoresearch	Cat# 115-295-003; RRID: AB_2338756
Alexa Fluor488-conjugated streptavidin	Jackson Immunoresearch	Cat# 016-540-084; RRID: AB_2337249
Chemicals, peptides, and recombinant proteins		
BSA	Sigma	A7906
EDTA	Sigma	607-429-00-8
PBS	VWR	E404-200 TABS
Tris-HCl	Sigma	T5941
NaCl	VWR	7647-14-5
MgCl2	Sigma	M2670
IGEPAL	Sigma	I8896
ARCTURUS PicoPure RNA isolation kit	Thermo Fisher Scientific	KIT0204
RNase-free DNase set	QIAGEN	79254
Bisbenzimide H33258	Sigma-Aldrich	Cat# B2883; CAS: 23491-45-4
Neurobiotin tracer	Vector Labs	Cat# SP-1120
FluoroJade C dye	Sigma	AG325
DPX mountant	VWR	360294H
ProLong Gold antifade mountant	ThermoFisher Scientific	P10144
Critical commercial assays		
Chromium single cell 3′ library & gel bead kit v2	10x Genomics	cat#: 120237 (v2)
Chromium i7 multiplex kit	10x Genomics	N/A
Chromium single cell A chip kit	10x Genomics	cat#: 120236
TruSeq stranded mRNA library prep kit	Illumina	cat#: RS-122-2101/2
HiSeq sequencing kit TruSeq v4	Illumina	cat#: FC-401-4003
RNAscope fluorescent multiplex reagent kit	ACD	320850
Deposited data		
LCM-RNA-seq	Gene Expression Omnibus (NCBI)	GSE143555
snRNA-seq	Gene Expression Omnibus (NCBI)	GSE143560
Experimental models: organisms/strains		
Mouse: Thy1.2-G-CaMP7-DsRed2	RIKEN Bioresources Center	stock RBRCO6579
Mouse: Calb1-2A-dgCre-D	Jackson Labs	N/A
Mouse: TdTomato reporter line Ai9	Jackson Labs	Stock No:007905
Rat: Wistar	Instituto Cajal Animal facility	N/A
Mouse: C57BL/6	Instituto Cajal Animal facility	N/A

(*Continued on next page*)

Continued

REAGENT or RESOURCE	SOURCE	IDENTIFIER
Oligonucleotides		
Wfs1-forw (5′CATCCCCAACAACCTGTTCC)	Sigma	NM_031823.1, bp 783-1631
Wfs1-rev (5′ACACCAGGTAGGGCACCACC)	Sigma	N/A
Ndst4-forw (5′ATACATCCAAAACTGATCCCAC)	Sigma	XM_006233274.2, bp 536-1024
Ndst4-rev (5′AAAAGCACTGGCTGGTAGGTAG)	Sigma	N/A
Syt17-forw (5′ACACATCCAAGTCCACATACAG)	Sigma	NM_138849.1, bp 378-1118
Syt17-rev (5′GTGTACCAGCTGGATTTTCACA)	Sigma	N/A
Hrt1a-forw (5′CTTTCTATATCCCGCTGTTGCT)	Sigma	J05276.1, bp 730-1663
Hrt1a-rev (5′CACACAGATACTAGTGGTTCTC)	Sigma	N/A
Scn7a-for (5′GATTATTTCTTCCCTTGTGTATGC)	Sigma	NM_131912.1, bp 2812-3550
Scn7a-rev (5′CTAAAGTCATCTTCGCTCAAGG)	Sigma	N/A
Recombinant DNA		
Mm-Spag5	ACD	505691
Mm-Dcc-C3	ACD	427491-C3
Mm-Dapk1-C3	ACD	880221-C3
RNAscope 3-plex positive control probe-Mm	ACD	320881
RNAscope 3-plex negative control probe	ACD	320871
Software and algorithms		
Sequencer Software HiSeq Control Software	Illumina, Inc	https://support.illumina.com/sequencing/sequencing_instruments/hiseq_2500/downloads.html?langsel=/us
R	R Foundation for Statistical Computing	https://www.R-project.org/; RRID: SCR_001905
RStudio	RStudio, PBC	https://www.rstudio.com/; RRID: SCR_000432
FastQC	Simon Andrews	https://www.bioinformatics.babraham.ac.uk/projects/fastqc; RRID: SCR_014583
STAR	Dobin et al., 2013	https://code.google.com/archive/p/rna-star; RRID: SCR_004463
Samtools	Li et al., 2009	http://samtools.sourceforge.net; RRID: SCR_002105
HTSeq	Anders et al., 2015	https://htseq.readthedocs.io/en/master/; RRID: SCR_005514
DESeq2	Love et al., 2014	http://www.bioconductor.org/packages/release/bioc/html/DESeq2.html; RRID: SCR_015687
Cell Ranger	Huang et al., 2009	https://david.ncifcrf.gov; RRID: SCR_017344
Seurat	Butler et al., 2018; Stuart et al., 2019	http://satijalab.org/seurat/; RRID: SCR_016341
Monocle 2	Qiu et al., 2017a, 2017b	http://cole-trapnell-lab.github.io/monocle-release; RRID: SCR_016339
DAVID Bioinformatics	Huang et al., 2009	https://david.ncifcrf.gov; RRID: SCR_001881
Webgestalt	Liao et al., 2019	http://www.webgestalt.org; RRID: SCR_006786
MATLAB 2016b	Mathworks	https://www.mathworks.com; RRID: SCR_001622
ImageJ	NIH Image	https://imagej.net/ImageJ; RRID: SCR_003070
SPSS Statistics	IBM	https://www.ibm.com/products/spss-statistics; RRID: SCR_002865
Other		
Resource website for the LCM RNA-seq data	This paper	http://lopezatalayalab.in.umh-csic.es/CA1_Sublayers_&_Epilepsy
Resource website for the snRNA-seq data	This paper	http://lopezatalayalab.in.umh-csic.es/CA1_SingleNuclei_&_Epilepsy
Silicon probes: 16-channel linear; 100 μm inter-spacing; 413 μm2 electrode area	Neuronexus	A1x16-5mm-100-413

RESOURCE AVAILABILITY

Lead contact

Further information and requests for reagents and resources may be directed to the lead contact, Dr. Liset M de la Prida (lmprida@cajal.csic.es).

Materials availability

This study did not generate any new unique reagents.

Data and code availability

No unpublished custom code, software or algorithm was used in this study. Freely available software and algorithms used for analysis are listed in the resource table. Some analyses were specifically designed for the purpose of this paper using routines written in MATLAB 7.10 (MathWorks). All custom scripts and data contained in this manuscript are available upon request from the Lead Contact. The accession number for the bulk-tissue transcriptome (LCM RNA-seq) and single-nuclei RNA-seq (snRNA-seq) data reported in this paper is Gene Expression Omnibus (GEO) database: GSE143555 (LCM RNA-seq) https://www.ncbi.nlm.nih.gov/geo/query/acc.cgi?acc=GSE143555; GSE143560 (snRNA-seq) https://www.ncbi.nlm.nih.gov/geo/query/acc.cgi?acc=GSE143560. Two open web applications provide visualization of transcriptomic data: LCM RNA-seq data: http://lopezatalayalab.in.umh-csic.es/CA1_Sublayers_&_Epilepsy. snRNA-seq data: http://lopezatalayalab.in.umh-csic.es/CA1_SingleNuclei_&_Epilepsy.

EXPERIMENTAL MODEL AND SUBJECT DETAILS

All experimental protocols and procedures were performed according to the Spanish legislation (R.D. 1201/2005 and L.32/2007), the European Communities Council Directives of 1986 (86/609/EEC) and 2003 (2003/65/CE) for animal research, and were approved by the Ethics Committee of the Instituto Cajal.

Adult male Wistar rats (180–200 g; 6-8 weeks postnatal), as well as wild-type C57 and transgenic mice (20-25 g; 8-9 weeks postnatal), were treated with multiple intraperitoneal injections of kainate (5 mg/kg) at hourly intervals until they reached *status* epilepticus. Transgenic mouse lines included the Thy1.2-G-CaMP7-DsRed2 (c57BL/6J-Tg(Thy1-G-CaMP7-DsRed2)492Bsi, stock RBRCO6579, RIKEN) and the Calb1-Cre (Jackson Lab, stock No:023531; Calb1-2A-dgCre-D) crossed with the tdTomato reporter line (Jackson Lab, stock No:007905; Ai9). The *status* was defined as a condition of continuous seizures lasting longer than 30 min. In a subset of rats, the lithium-pilocarpine model was used. These rats were i.p. injected with pilocarpine hydrochloride 12–24 h after the injection of lithium chloride (127 mg/kg, i.p.). Between one and four doses of 10 mg/kg pilocarpine were injected every 30 min until the *status* epilepticus was reached. Diazepam (4 mg/kg) was injected 1 h post-*status* to stop convulsions in all animals. They received intraperitoneal injections of 5% dextrose in saline (2.5 ml) and their diet was supplemented with fruit and powder milk during the following 2–3 days. After 3 days, animals behaved normally and were housed individually. Control animals were injected with saline and received treatments similar to epileptic animals.

Animals used in this study were examined in the chronic phase of the *status epilepticus* model of TLE (2-23 weeks post-*status*) when they already exhibited spontaneous seizures and interictal discharges (IID) (Figures S1A and S1B). In epileptic rats and mice, these events were typically associated with high-frequency oscillations (HFOs; Figure S1B), which are considered biomarkers of epileptogenesis (Jefferys et al., 2012; Valero et al., 2017). We focused on the dorsal hippocampus given the major role in associated cognitive comorbidities of epilepsy and more consistent neuronal loss as compared to ventral (Thom et al., 2012; Valero et al., 2017). In some epileptic animals, we aimed to induce convulsive seizures using high-pitched sounds (pulses of 95-100 dB and 1-20 s duration at random intervals of 1-20 s during 10 min). A convulsive motor seizure was defined according to clinical criteria, as sustained and repeated forelimbs automatisms with or without falling. Control animals did never exhibit convulsive seizures using this protocol.

METHOD DETAILS

EEG recordings and analysis

To evaluate epileptogenesis, some rats and mice were implanted with either intracranial 16-channel silicon probes or skull EEG-grid of 32-channels (Neuronexus) under isoflurane anesthesia (1.5%–2% mixed in oxygen 400–800 ml/min). Jeweler's screws were inserted into the skull for providing additional anchoring and reference/ground connections (over the cerebellum). The implant was secured with dental cement. Animals were recovered from anesthesia and returned to home cages.

For recordings, EEG signals were pre-amplified (4x gain) and recorded with a 32-channel AC amplifier (Axona), further amplified by 100, filtered by analog means at 1 Hz to 5 kHz, and sampled at 20 kHz/channel with 12 bits precision. EEG recordings were synchronized with a ceiling video camera (30 frames/s) to track the animal position in space.

Analysis of electrophysiological signals was implemented in MATLAB 9.3 (MathWorks). EEG signals from the frontal and parietal electrodes were used to identify theta periods during running (band-pass 4-12 Hz) and periods of immobility characterized by low frequency delta activity (0.5-4 Hz). Forward-backward-zero-phase finite impulse response (FIR) filters of order 512 were used to

preserve temporal relationships between channels and signals. Spectral values fitted to 1/f were similar between groups for frequencies > 150 Hz. HFO events were defined from the bandpass filtered signal (80-120 Hz) by thresholding (> 4 SDs). The power spectra were evaluated in a window of ± 0.2 ms around each detected event. Time-frequency analysis was performed by applying the multitaper spectral estimation in sliding windows with 97.7% overlap and frequency resolution of 10 Hz in the 90-600 Hz frequency range. HFO activity was evaluated as the power integral in the 80-120 Hz band.

We used a combination of features to identify HFO events automatically and to classify them in different categories (Valero et al., 2017) (Figure S1). First, we identified large amplitude transient (< 100 ms) discharges using LFP and current-source-density signals (CSD, i.e., the second spatial derivative) at the SR and SLM. Second, we identified HFO events at the SP by frequency thresholding over 100 Hz. Then we used spectral indices such as entropy and fast ripple indices from candidate HFO events at SP together with amplitude information from LFP and CSD signals at SR to classify events as: a) SPW-ripples (low amplitude; 100-150 Hz); b) SPW-fast ripples (medium amplitude, > 150 Hz) and IID-HFO (larger amplitude, > 100 Hz). Events not meeting criteria were left unclassified. Surface EEG recordings from mice were analyzed similarly, by using channels over the dorsal hippocampus or at the frontal cortex to identify HFO events and channels over the parietal cortex using selected segments of the EEG.

In vivo recording and labeling of single cells

Rats were anesthetized with urethane (1.2 g/kg, i.p.), fastened to the stereotaxic frame and warmed to keep their body temperature at 37°C. Two bilateral craniotomies of ~1 mm diameter were performed for CA3 stimulation (AP: −1.2 mm, ML: 2.9 mm) and CA1 recordings (AP: −3.7 mm; ML: 3 mm). The dura was gently removed, the *cisterna magna* was drained and the craniotomy covered with warm agar to reinforce stability.

A 16-channel silicon probes (NeuroNexus Tech; 100 μm interspaced, 413 μm^2 contact) was advanced perpendicular along the CA1-DG-CA3c axis guided by extracellular stimulation and electrophysiological hallmarks. Concentric bipolar electrodes were advanced 3.5 mm with 30° in the coronal plane to stimulate CA3. Stimulation consisted of biphasic square pulses (0.2 ms duration, 0.05-1.2 mA every 5 s). Extracellular signals were pre-amplified (4x gain) and recorded with a 16(32)-channel AC amplifier (Multichannel Systems), further amplified by 100, analogically filtered at 1Hz to 5 kHz, and sampled at 20 kHz/channel with 12 bits precision with a Digidata 1440. A subcutaneous Ag/AgCl wire in the neck served as reference. Recording and stimulus position was confirmed by post hoc histological analysis.

Intracellular recording and labeling were obtained in current-clamp mode using sharp pipettes (1.5 mm/0.86 mm outer/inner diameter borosilicate glass; A-M Systems, Inc) filled with 1.5 M potassium acetate and 2% Neurobiotin (Vector Labs, Inc; 50-100 MΩ) (Cid and de la Prida, 2019). Signals were acquired with an intracellular amplifier (Axoclamp 900A) at 100x gain. The resting potential, input resistance and amplitude of action potentials was monitored all over the course of experiments.

After data collection, Neurobiotin was ejected using 500 ms depolarizing pulses at 1-3 nA at 1 Hz for 10-45 min. Animals were perfused with 4% paraformaldehyde (PFA) and 15% saturated picric acid in 0.1 M, pH 7.4 phosphate buffered saline (PBS). Brains were postfixed overnight at room temperature (RT), washed in PBS and serially cut in 70 μm coronal sections (Leica VT 1000S vibratome). Sections containing the stimulus and probe tracks were identified with a stereomicroscope (S8APO, Leica). Sections containing Neurobiotin-labeled cells were localized by incubating them in 1:400 Alexa Fluor 488-conjugated streptavidin (Jackson ImmunoResearch 016-540-084) with 1% Triton X-100 in PBS (PBS-Tx) for 2 hours at room temperature (RT). To evaluate morphological features of single cells, sections containing the somata of recorded cells were processed with Triton 1% in PBS, blocked with 10% fetal bovine serum (FBS) in PBS-Tx and incubated overnight at RT with the primary antibody solution containing rabbit anti-Calbindin (1:500, CB D-28k, Swant CB-38) or mouse anti-Calbindin (1:1000, CB D-28k, Swant 300) antibodies with 1% FBS in PBS-Tx. After three washes in PBS-Tx, sections were incubated for 2 hours at RT with appropriate secondary antibodies: goat anti-rabbit Alexa Fluor 633 (1:500, Invitrogen, A21070), and goat anti-mouse Alexa Fluor488 (Jackson Immunoresearch, 115-545-003) or goat anti-mouse Rhodamine Red (1:200, Jackson ImmunoResearch, 115-295-003) in PBS-Tx-1% FBS. Following 10 min incubation with bisbenzimide H33258 (1:10000 in PBS, Sigma, B2883) for nuclei labeling, sections were washed and mounted on glass slides in Mowiol (17% polyvinyl alcohol 4-88, 33% glycerin and 2% thimerosal in PBS).

All morphological analyses were performed blindly to electrophysiological data. The distance from the cell soma to radiatum was measured from confocal images using information from Calbindin and bisbenzimide staining. All pyramidal cells included in this study were localized within the CA1 region. Calbindin immunostaining was used to estimate the width of the superficial sub-layer from the border to the stratum radiatum. Superficial cells were defined based on the location of the soma within the calbindin sublayer, independently on their immunoreactivity (Valero et al., 2015). The border with radiatum was estimated for each section and the distance from the recorded cell somata was measured using ImageJ (NIH Image).

Analysis of intracellular single-cell recordings

Interictal discharges and sharp-waves associated with HFO events (ripples or fast ripples) recorded simultaneously to the intracellular membrane potential were detected as explained before. The timing of these events was used to identify the corresponding membrane potential deflections. Time-frequency analysis of HFO events was performed by applying the multitaper spectral estimation in sliding windows with 97.7% overlap and frequency resolution of 10 Hz in the 90-600 Hz frequency range (only the 100-600 Hz range is shown) to data sweeps aligned by sharp-wave ripple events (±1 s). Membrane potential responses of single-cells were evaluated in peri-event plots before (−200 to −150 ms), during (±50 ms) and after (150 to 200 ms) HFO events.

Passive electrophysiological properties (input resistance, membrane decay and capacitance) of neurons recorded intracellularly *in vivo* were measured using 500 ms currents step in current-clamp mode. Cells with intracellular action potential amplitude smaller than 40 mV were excluded. Resting membrane potential and input resistance were estimated by linear regression between baseline potential data and the associated holding current. Intrinsic firing properties, including action potential threshold, half-width duration and AHP were estimated from the first spike in response to depolarizing current pulses of 0.2 nA amplitude and 500 ms duration. The sag and maximal firing rate were calculated from current pulses of ± 0.3 nA amplitude. A bursting index was defined as the ratio of the number of complex spikes (minimum of 3 spikes < 8 ms inter-spike interval) over the total number of spikes recorded during theta activity.

cFos immunostaining and analysis

To evaluate immediate-early gene expression associated to sound-induced convulsive seizures, animals were perfused 1 hour after and their brains cut in 70 μm coronal sections. Selected sections were stained against c-Fos using a polyclonal antibody at 1:250 (Santa Cruz Biotechnology sC-52) and bisbenzimide. Using one 20x confocal mosaic per animal, we quantified cFos intensity at CA1 pyramidal cells by delineating single-cell nuclei stained with bisbenzimide in one confocal plane (ImageJ). The mean intensity of cFos signal from each cell was then normalized by subtracting the background (set at 0) and dividing by the maximal positive signal in the mosaic, which was always at granule cell level (set at 1). No significant differences of background were observed across sections. Delineated cells were ranked by their distance to radiatum to classify them as deep or superficial, according to standard measurements of Calb1-layer thickness.

Laser capture microdissection (LCM) and RNA isolation

Brains from 3 control and 3 epileptic rats were dissected, longitudinally cut in half (separating both hemispheres), wrapped in aluminum foil and immediately frozen in liquid nitrogen. To avoid circadian effects on gene expression all samples were collected in the morning before noon and conserved at −80°C until use. The hippocampal region of each hemisphere was cut in 20 μm slices in a cryostat (Leica) (chamber temperature: −20°C; block temperature: −30°C) and placed on 1.0 mm PEN-membrane covered slides (Carl Zeiss). Slides were conserved at −20°C until use. Right before microdissection, slides were dried with vapor of liquid nitrogen. The CA1 cell layer was microdissected with a Leica 6000 laser microdissector through a 40x non-oil immersion objective to obtain cell bodies of superficial and deep sublayers separately (Figure 2A). Microdissected deep and superficial areas were collected in different empty caps of 0.5 mL Eppendorf tubes. After microdissection, samples were processed following ARCTURUS PicoPure RNA Isolation Kit (Thermo Fisher Scientific) instructions in order to extract and isolate total RNA. Briefly, 50 μl of extraction buffer was added into the cap, incubated at 42°C for 30 min, centrifuged at 800 x G for 2 min and stored at −80°C. The same volume of 70% ethanol was added to the cell extract and the mixture was pipetted into a pre-conditioned RNA purification column. The column was centrifuged 2 min at 100 x G and 30 s at 16000 x G, and washed with 100 μl of Wash Buffer 1. To completely eliminate DNA, the purification column was treated with 40 μl of DNase (diluted 1/8 in RDD Buffer) (QIAGEN), incubated 15 min and centrifuged at 8000 x G for 15 s. Then the column was washed twice with 100 μl of Wash Buffer 2, and centrifuged at 8000 x G after the first wash and at 16000 x G after the second one. Finally, RNA was eluted into a new 0.5 μl Eppendorf tube by adding 11 μl of elution buffer onto the column membrane, incubating the column for 1 min at room temperature, and centrifuging the column for 1 min at 1000 x G and at 16000 x G immediately after. Total RNA samples were stored at −80°C. RNA integrity number (RIN) was similar in control (4.7 ± 0.8) and epileptic rats (5.7 ± 0.5; p = 0.07; 3 replicates x 2 sublayers per group), as well as for deep (5.2 ± 0.9) and superficial sublayers (5.3 ± 0.1; p = 0.81; n = 6 replicates per sublayers).

LCM RNA-seq library construction and sequencing

RNA preparation for sequencing deep and superficial CA1 sublayers from control and epileptic rats was performed as described in Scandaglia et al. (2017). The twelve samples were sequenced according to manufacturer instructions in a HiSeq2500 sequencer (Illumina, Inc). Libraries were strand specific (reverse) and sequenciation was performed in paired-end configuration with a read length of 75 bp. Library size of read pairs for the different samples analyzed was between 47 and 59 Million reads. RNA-seq data can be accessed at the GEO repository (GSE143555).

LCM RNA-seq data analysis

Alignment quality control of sequenced samples (LCM RNA-seq) was assessed with FastQC (v.0.11.3) (Babraham Institute) and RNA-seq tracks were visualized using IGV (v.2.3.57) (Thorvaldsdóttir et al., 2013). LCM RNA-seq reads were mapped to the rat genome (Rnor_6.0.83) using STAR (v.2.5.0c) (Dobin et al., 2013), and files were further processed with Samtools (v.0.1.19). Aligned reads were counted to gene transcripts using HTSeq (v.0.6.1) (Anders et al., 2015). Differential expression analysis was performed using DESeq2 (v.1.10.0) (Love et al., 2014) of the bioconductor suite (Huber et al., 2015) in the R (v.3.2.2) statistical computing platform. The experimental design consisted in two factors (treatment and anatomical area) and there was also grouped samples (samples from different anatomical areas (minus (deep) and plus (superficial) that were obtained from individual mice). Genes were considered differentially expressed at Benjamini-Hochberg (BH) adj. $p < 0.05$ and $FC > 0.3$ (Benjamini and Hochberg, 1995), except otherwise specified. GO analysis was performed using DAVID (v.6.8) bioinformatics platform (Huang et al., 2009).

LCM RNA-seq single-cell informed data analysis

Single-cell RNA-seq data from Zeisel et al. (2015) was reanalyzed with consensus cluster SC3 algorithm (Kiselev et al., 2017). From the original 3,005 cells, pyramidal and interneurons were removed from somatosensory cortex, resulting in a total of 2,442 cells. Remaining cells were re-analyzed downstream with SC3. Clustering stability was optimal for 6 clusters. One cluster presented high heterogeneity (mixed population cluster), and was reanalyzed with the optimal clustering stability (5 clusters). Marker genes were tested for every cluster with Wilcoxon signed rank test. Top 10 genes with the area under the receiver operating characteristic (ROC) curve (AUC) power > 0.85 and with the adj. $p < 0.01$ from both cluster analyses were selected, with a total of 69 bona fide population markers. Based on the markers, populations were fused/splitted and 3 populations were isolated in the first clustering (pyramidal neurons, interneurons and oligodendrocytes) and 4 more in the second (astrocytes, endothelial cells, microglia and mural cells). Sixteen outlier cells were removed by total_counts, total_features or pct_counts_spike criteria, remaining 2,426 cells with a high correspondence with the original classification: Astrocytes (155 cells), Endothelial (177 cells), Interneurons (174 cells), Microglia (85 cells), Mural (56 cells), Oligodendrocytes (804 cells) and Pyramidal (975 cells). Next, to capture convoluted gene signatures on LCM RNA-seq we used gene sets of equal size that were differentially regulated between superficial and deep sublayers of control and epileptic rats. To obtain these gene sets, we first filtered the genes by significance (adj. $p < 0.1$), then significantly differentially regulated genes were ranked by fold-change, and top 250 differentially regulated genes for each sublayer and condition, were retained for further analysis. We then, obtained normalized gene expression from scRNA-seq data for these gene sets and performed linear dimensionality reduction by principal component analysis to summarize and visualize the cells in the low-dimensional space. We also performed Pearson pairwise correlation and hierarchical clustering for these gene sets across all cells, to capture cell-type specific gene signatures that were mapped to major cell types in CA1 by using previously identified cell markers.

Single-cell RNA-seq data from Allen Brain Map portal - Mouse Whole Cortex and Hippocampus SMART-seq (2019) with 10x-SMART-seq taxonomy (2020) (http://portal.brain-map.org/atlases-and-data/rnaseq/mouse-whole-cortex-and-hippocampus-smart-seq) was downloaded and subsetted as follows: from the original 76,533 cells, cells from hippocampal region were retained, and subsequently, cells from CA2, CA3, DG or empty subclass were removed. Then, cells of subclasses Astro, Micro-PVM, Endo, Oligo or VLMC were added. This initial filtering led a total of 5,506 cells. Of these, cells tagged by subclass as CA1-ProS (1,592 cells), Astro (976 cells), Lamp5 (864 cells), Vip (462 cells), Sncg (416 cells), Sst (266 cells), Oligo (236 cells), Endo (213 cells), Micro-PVM (176 cells), VLMC (159 cells), Pvalb (69 cells) were retained for further analysis, while cells tagged by subclass as SUB-ProS (29 cells), L2 IT RHP (21), NP SUB (9), L2/3 IT CTX-1 (3), L5 IT TPE-ENT (3), Sst Chodl (3), L2/3 IT ENTl (2), L6 CT CTX (2), Meis2 (2), L2/3 IT CTX-2 (1), L2/3 IT PPP (1), L6b CTX (1) were removed because of their low cell number and/or mismatch with CA1 or glial cells. The remaining 5,429 cells were grouped in their corresponding major cell populations as follows: Astrocytes (Astro) (976 cells), Endothelial (Endo) (213 cells), Interneurons (Lamp5, Pvalb, Sncg, Sst, Vip) (2077 cells), Microglia (Micro-PVM) (176 cells), Mural (VLMC) (159 cells), Oligodendrocytes (Oligo) (236 cells) and Pyramidal (CA1-ProS) (1,592 cells). Next, we proceed as indicated before to capture convoluted gene signatures on LCM RNA-seq by using normalized expression data from this scRNA-seq dataset, for differentially regulated between superficial and deep sublayers of control and epileptic rats.

Single-nuclei isolation

We accurately isolated single nuclei from 2 control and 2 epileptic Calb1::CrexTdTomato young adult mice. We used these animals to facilitate identification of the CA1 region under a fluorescent scope. Animals were sacrificed 12 weeks after the kainate/saline administration by cervical dislocation and brains were dissected and cut in 300 um thick slices in a vibratome covered by ice cold HBBS 1x. As in LCM studies, samples were collected before noon to avoid circadian effects. The dorsal CA1 region were manually dissected from 4 consecutive slices and put altogether into 400 μL of ice-cold MACS buffer (0,5% BSA, 2 mM EDTA, PBS 1x). CA1 portions were transferred to a dounce homogenizer (20404 Lab Unlimited) containing 400 μL of MACS buffer and were homogenized 12-15 times each with the pestle. The cell suspension was transferred to a 2 mL Eppendorf tube and centrifuge 15 min 500 x G 4°C. Cell pellets were resuspended in 500 μL of lysis buffer (10 mM Tris-HCL, 10 mM NaCl, 3 mM $MgCl_2$, 0,1% IGEPAL) and kept 5 min on ice. Samples were then spun down at 500 x G for 30 min in a pre-chilled centrifuge. The nuclei pellet was resuspended in PBS 1x 1% BSA and then 15,000 nuclei were purified by flow cytometry in a BD FACS Aria III. The whole process was carried out at 4°C.

Single-nucleus RNA sequencing

Purified intact nuclei from mouse hippocampal CA1 area were processed through all steps to generate stable cDNA libraries. For every sample, 15,000 nuclei were loaded into a Chromium Single Cell A Chip (10x Genomics) and processed following the manufacturer's instructions. Single-nuclei RNA-seq libraries were prepared using the Chromium Single Cell 3′ Library & Gel Bead kit v2 and i7 Multiplex kit (10x Genomics). Pooled libraries were then loaded on a HiSeq2500 instrument (Illumina) and sequenced to obtain 75 bp paired-end reads following manufacturer instructions. On sequencing depth, 262 million fragments were generated for the control condition and 296 for the epileptic dataset. Libraries reached a sequencing saturation of 86.9% for control and 91.2% for epilepsy condition. snRNA-seq data can be accessed at the GEO repository (GSE143560).

snRNA-seq analysis

Quality control of sequenced reads was performed using FastQC (Babraham Institute). Sequenced samples were processed using the Cell Ranger (v.2.2.0) pipeline (10x Genomics) and aligned to the GRCm38 (mm10) mouse reference genome customized to count

reads in introns (pre-mRNA) over the Ensembl gene annotation version 94. Barcodes with total unique molecular identifier (UMI) count > 10% of the 99th percentile of the expected recovered cells were selected for further analysis. Using this criterion, we retrieved 3,661 (control), 3,078 (epileptic) high quality nuclei per sample. Mean reads per nucleus were 71,449 (control) and 96,150 (epileptic). Median genes per nucleus were 71,449 (control) and 96,150 (epileptic). Minimum UMI count per nucleus were 710 (control), 540 (epileptic), well above the typical quality standards in single-cell/nucleus sequencing. Single-nucleus RNA-seq data were subsequently pre-processed and further analyzed in R (v.3.4.4) using Seurat (v.2.3.4) (Butler et al., 2018; Stuart et al., 2019). Filtering parameters were as follows: genes, nCell < 5; cells, nGene < 200. Data were then normalized using global-scaling normalization (method: LogNormalize, scale.factor = 10,000).

An initial exploratory analysis was performed on each dataset separately. This analysis retrieved a similar number of clusters in each dataset that were approximately equal in size. We next combined both datasets using the function MergeSeurat. Highly variable genes (HVGs) were detected using FindVariableGenes function with default parameters. Then, normalized counts on HVGs were scaled and centered using ScaleData function with default parameters. Principal component analysis (PCA) was performed over the first ranked 1,000 HVGs. Plots of the two principal components of the PCA, where cells were colored by dataset, excluded the presence of batch effects. Cluster detection was carried out with Louvain algorithm in FindClusters function, using 20 first PCA dimensions and resolution of 0.6 (the default number in Seurat and the optimal according to cell number, data dispersion and co-expression of previously reported cell markers). Plots of the two principal components of the PCA where cells were colored by dataset of origin excluded the presence of batch effects.

This analysis identified 13 clusters. CA1 pyramidal neurons populated three of these clusters: one cluster was enriched in bona fide gene markers of deep cells (*Ndst4*, *Coll11a1*) whereas a second one was enriched in canonical markers of superficial cells (*Calb1*, *Epha3*). The third cluster showed a mixed identity. An additional round of clustering segmented this population in three additional clusters that were enriched in deep and superficial markers, respectively, and a third cluster that could not be annotated based on the presence of gene markers of CA1 sublayer neurons. The vast majority of cells within this cluster (66/67) were from epileptic mice (Pyr_ES). Next, the FindMarkers function was used to identify gene markers and to determine the cell populations represented by each cluster. Finally, cell subtypes were manually aggregated based on the presence of canonical markers of known cell types into six distinct major cell types: excitatory neurons (Excit); inhibitory neurons (Inter); oligodendrocytes (ODC); oligodendrocyte progenitor cells (OPCs); microglia (Microglia); astrocytes (Astro).

Visualization and embedding were performed using stochastic nearest neighbors (tSNE) (van der Maaten and Hinton, 2009) and uniform manifold approximation and projection (UMAP) (McInnes et al., 2018) methods over PCA using the 20 first PCA dimensions. UMAP plots of gene expression show normalized count (UMIs) per nucleus. The equalized expression between fixed percentiles was plotted according to the following criterion: the minimum expression was adjusted to 5% and the maximum expression was adjusted to 95% in all UMAP expression plots. To evaluate effects of epilepsy, datasets from both conditions were merged and HVGs were identified for each dataset as above indicated. Only HVGs that were detected in all datasets were used to perform visualization and embedding as described above. Clustering was performed on merged dataset from both conditions and populations were identified combining these results with clustering information obtained in control and epileptic datasets separately, together with co-expression of population markers.

Differential expression analysis (DEA) was used to identify population gene markers. For DEA, the nuclei of each population were contrasted against all the other nuclei in the merged dataset using Wilcoxon Rank Sum test on normalized counts. For epilepsy effect analysis, in the merged dataset, the nuclei of each population from the epileptic dataset were contrasted against all the other nuclei of the same population in control using Wilcoxon Rank Sum test on normalized counts. GO functional enrichment analyses were performed using DAVID (v.6.8) bioinformatics platform (Huang et al., 2009). All DEA and functional enrichment analyses applies False Discovery Rate (FDR) method by BH post hoc p adjustment, except otherwise specified.

Cell trajectories and pseudotime analysis

The disease pseudotime analysis was performed using Monocle 2 (v.2.8.0) (Qiu et al., 2017a, 2017b). First, the Seurat merged dataset was transformed to Monocle object and cells from Pyr_CA1 were subset. The size factor and dispersion of the subset was estimated, and data was normalized and preprocessed. Genes under the minimum level detection threshold of 0.1 and detected in less than 10 cells were filtered with the function setOrderingFilter. Genes defining how a cell progress through a pseudo-time disease trajectory were selected with the function differentialGeneTest (Monocle's main differential analysis routine). 2,579 genes (64,68% of a total of 3,987 genes considered as expressed) were significative with FDR adj. p < 1% for the combination of factors: ~SeuratCluster+Condition, and thus, defined the high dimensional space for pseudotemporal trajectory analysis.

Discriminative dimensionality reduction with trees (DDRTree) reduction algorithm learns the principal graph and specifies the trajectory. DDRTree was applied inside the function reduceDimension, and got the default parameters: norm_method = "log," pseudo_expr = 1, relative_expr = TRUE, auto_param_selection = TRUE (automatically calculate the proper value for the ncenter (number of centroids)) and scaling = TRUE (scale each gene before running trajectory reconstruction). Prior the dimensional reduction, the function reduceDimension also performed a variance-stabilization of the data (because the expressionFamily of the data was negbinomial.size). Finally, the cells were ordered according to pseudo-time with the function orderCells, which added a pseudo-time value and state for each cell; together encode where each cell maps to the trajectory.

For enrichment analysis on pseudotime trajectories, top-ranked 250 branched expression analysis modeling (BEAM) significant changes through the progression across the disease trajectory for each sublayer were clusterized and GO enrichment analyses on upregulated and downregulated clusters were performed using DAVID (v.6.8) bioinformatics platform (Huang et al., 2009).

Cell-type immunostaining and analysis

To evaluate the contribution of different cell-types to hippocampal sclerosis, control and epileptic rats and mice were perfused with 4% paraformaldehyde (PFA) and 15% saturated picric acid in 0.1 M PBS, pH 7.4. Brains were postfixed overnight and cut in 70 μm coronal sections (Leica VT 1000S vibratome). Sections containing the dorsal-intermediate hippocampus were processed with Triton 1% in PBS and blocked with 10% fetal bovine serum (FBS) in PBS-Tx. Sections were incubated overnight at RT with 1% FBS PBS-Tx solution containing primary antibodies against a battery of cell-type specific markers. The list of antibodies includes: rabbit anti-calbindin (1:1000, CB D-28k, Swant CB-38) or mouse anti-calbindin (1:500, CB D-28k, Swant 300) to identify superficial CA1 pyramidal cells; rabbit anti-Wfs1 (1:500, Protein Tech, 11558-1-AP) for CA1 pyramidal cells; rabbit anti-Iba1 (1:1000, Wako, 019-19741) for microglia; rabbit anti-GFAP (1:1000, Sigma, G9269) for astrocytes; rabbit anti-Olig2 (1:200, Millipore, AB9610) for oligodendrocytes. After three washes in PBS-Tx, sections were incubated for 2 hours at RT with appropriate secondary antibodies: goat anti-rabbit Alexa Fluor633 (1:200, ThermoFisher, A-21070), and donkey anti-mouse Alexa Fluor488 (1:200, ThermoFisher, A-21202) or goat anti-mouse Rhodamine Red (1:200, Jackson ImmunoResearch, 115-295-003) in PBS-Tx-1%FBS. Following 10 min incubation with bisbenzimide H33258 (1:10000 in PBS, Sigma, B2883) for nuclei labeling, sections were washed and mounted on glass slides in Mowiol (17% polyvinyl alcohol 4-88, 33% glycerin and 2% thimerosal in PBS).

To acquire multichannel fluorescence stacks from recorded cells, a confocal microscope (Leica SP5) with LAS AF software v2.6.0 build 7266 (Leica) was used. The following channels (fluorophore, laser and excitation wavelength, emission spectral filter) were used: a) bisbenzimide, Diode 405 nm, 415–485 nm; b) Alexa Fluor 488 nm, Argon 488 nm, 499–535 nm; c) Rhodamine Red / Alexa Fluor 568 / Texas Red, DPSS 561 nm, 571–620 nm; d) Alexa Fluor 633, HeNe 633 nm, 652–738 nm; and objectives HC PL APO CS 10.0 × 0.40 DRY UV, HCX PL APO lambda blue 20.0 × 0.70 IMM UV and HCX PL APO CS 40.0 × 1.25 OIL UV were used.

FluoroJade staining

To evaluate neurodegenerating neurons we used coronal sections from epileptic rats perfused at different time points post-*status*. Selected sections were immunostained against Wfs1 followed by FluoroJade staining. To this purpose, sections were pretreated for 5 min with 1% sodium hydroxide in 80% ethanol, followed by 70% ethanol (2 min) and distilled water (2 min). Sections were then incubated 10 min in 0.06% potassium permanganate, rinsed in distilled water and immersed into 0.0001% solution of FluoroJade C dye (Sigma AG325) in 0.1% acetic acid (pH 3.5) for 10 min. After a brief wash in distilled water, they were mounted on gelatin-coated slides, air-dried, coverslipped with DPX and examined under a confocal microscope as described above. FluoroJade positive cells exhibited bright green fluorescence.

In situ hybridization analysis

Selected sections from control and epileptic rats were processed for *in situ* hybridization using standard methods. Briefly, riboprobes were prepared from Rat *Enpp2* cDNA (Image clone ID 7115236) and using RT-PCR from rat adult hippocampus to prepare *Wfs1* (NM_031823.1, from bp 783 to 1631), *Ndst4* (XM_006233274.2, from bp 536 to 1024), *Syt17* (NM_138849.1, from bp 378 to 1118), *Hrt1a* (J05276.1, from bp 730 to 1663) and *Scn7a* (NM_131912.1, from bp 2812 to 3550) cDNAs. Similar riboprobes were used in sections from normal and epileptic mice. Riboprobe hybridization was detected using alkaline phosphatase–coupled anti-digoxigenin Fab fragments (Sigma). Hybridized sections were mounted in glycerol and photographed using a Nikon stereoscope and a DCC Nikon camera.

RNAscope analysis

Control and epileptic mice were perfused with 4% paraformaldehyde (PFA) and 15% saturated picric acid in 0.1 M PBS, pH 7.4. Brains were post-fixed overnight and cut in 50 μm coronal sections (Leica VT 1000S vibratome) which were kept at −20°C in a solution of 30% glycerol and 30% etylenglycol in PBS. RNAscope Fluorescent Multiplex Assay (Advanced Cell Diagnostics) was carried out according to the manufacturer's protocols. Briefly, sections containing the dorsal-intermediate hippocampus (around −2 μm AP from Bregma) were washed in PBS-Tx, and mounted onto SuperFrost Plus microscope slides (10149870, ThermoFisher Scientific). They were then dehydrated at 60°C follow by ethanol, pretreated with a target retrieval solution (322000, ACD) and protease III (322340, ACD), and co-hybridized with *Spag5* (Mm-Spag5, 505691, ACD) and *Dcc* (Mm-Dcc-C3, 427491, ACD) or *Dapk1* (Mm-Dapk1-C3, 880221-C3, ACD) probes. Finally, the amplification steps (RNAscope Fluorescent Multiplex Detection reagents, 320851, ACD) were followed, using Atto 550 for *Spag5* and Atto 647 for *Dcc* or *Dapk1* as fluorescent labels. The RNAscope 3-plex positive control probe set (320881, ACD), with probes to Polr2a, PPIB and UBC, was used to confirm preservation of sample RNA. The negative control probe to bacterial DapB (320871) was used to establish non-specific labeling.

Following the RNAscope protocol, sections were blocked for 30 min with 10% FBS in PBS-Tx, and incubated overnight at RT with rabbit anti-Wfs1 (1:500, Protein Tech, 11558-1-AP) in 1% FBS PBS-Tx. After three washes in PBS, sections were incubated for 2 h with donkey anti-rabbit Alexa Fluor488 (1:200, ThermoFisher Scientific, A-21206) in 1% FBS PBS-Tx, washed twice in PBS and mounted using ProLong Gold Antifade mountant (ThermoFisher Scientific, P10144).

Multichannel fluorescence stacks were achieved in a confocal microscope (Leica SP5) with LAS AF software v2.6.0 build 7266 (Leica), with a 40x objective (HCX PL APO CS 40.0 × 1.25 OIL UV), at 0.5 μm z-interval. Pinhole was set at 1 Airy, and following channels settings were applied for each fluorophore (excitation wavelength, emission spectral filter): Argon (488 nm, 499–553 nm) for Alexa Fluor488, DPSS (561 nm, 570–630 nm) for Atto 550, and HeNe (633 nm, 645–740 nm) for Atto 647. Diode (405 nm, 415–485 nm) was used as an unstained channel to identify autofluorescent material, which can be abundant in epileptic tissue. Images were acquired at 8 bits, 387.5 × 387.5 μm (1024 × 1024 pixels) in size. Brightness and contrast were adjusted with the ImageJ Fiji software (NIH Image).

To estimate the amount of *Dapk1*, *Spag5* and *Dcc* transcripts per cell, a total of 5 control and 5 epileptic animals (12 cells per animal) were analyzed. Each ROI was drawn in one confocal plane as the outline of a pyramidal cell soma at their maximum diameter based on Wfs1 immunoreactivity, using ImageJ. Only those cells focused within the first 10 μm were selected to avoid reduction of the signal due to depth in the section. In either *Dapk1*, *Spag5* or *Dcc* channels, single signal dots were counted, and clusters were converted to dot number as suggested by the manufacturer (ACD): (total intensity - average background intensity x area)/single dot average intensity.

QUANTIFICATION AND STATISTICAL ANALYSIS

Statistical analyses were performed with MATLAB, SPPSS and using the computing environment R (R Development Core Team, 2005, http://www.R-project.org). No statistical method was used to predetermine sample sizes. Normality and homoscedasticity were evaluated with the Kolmogorov–Smirnov and Levene's tests, respectively. The exact number of replications for each experiment is detailed in text and figures. Several ways ANOVAs or Friedman tests were applied. Post hoc comparisons were evaluated with the Tukey-Kramer, Student or Wilcoxon tests. Deep-superficial trends were evaluated using Spearman correlation and tested against 0 (i.e., no correlation was the null hypothesis) at $p < 0.05$ (two sided).